ISSN 0377-9416

PMAI

TRANSACTIONS OF POWDER METALLURGY ASSOCIATION OF INDIA

Vol. 35, December 2009

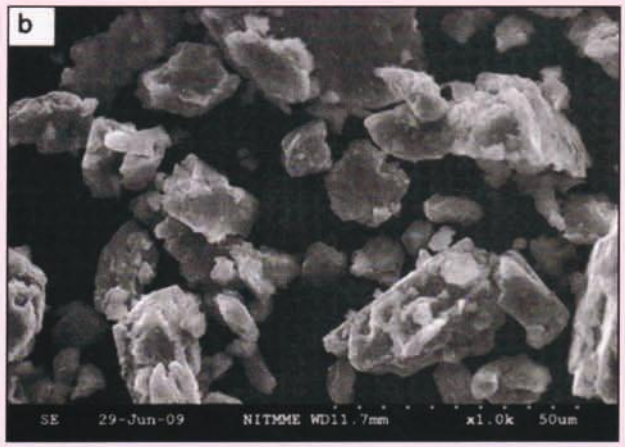

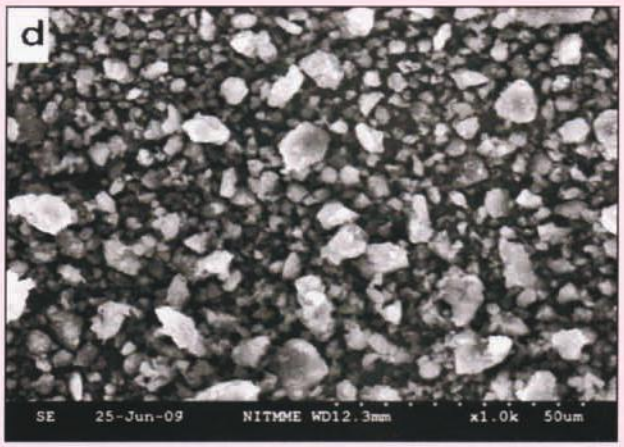

Editor
P.RAMAKRISHNAN

PMAI

Powder Metallurgy Association of India

TRANSACTIONS OF POWDER METALLURGY ASSOCIATION OF INDIA

Vol. 35, December 2009

Editor
P. RAMAKRISHNAN

Powder Metallurgy Association of India

Office Bearers

Vol. 35, December 2009

Published by

PMAI

Powder Metallurgy Association of India (PMAI), Mumbai
1002, B Wing, Kingston, High Street, Hiranandani Complex,
Near D-Mart, Powai Mumbai. Tel. : 25704588 / Email : pmai_pm@yahoo.com

Note : Neither the Powder Metallurgy Association of India nor the editor assumes responsibility of opinions expressed by the authors of the papers published in this transaction.

Price : Rs. 300/- for Indian subscribers and US $ 50 for Overseas subscribers.

Cover : AA 4032 Alloy Powders

Editorial

The 5th. International Conference & Trade Exhibition on High Performance Materials by Powder Metallurgy for Automotive and Engineering Industries and 35th.Annual Technical Meeting of Powder Metallurgy Association of India, was held during Feb. 16-18, 2009 at Cidade De Goa Resort, Vainguinim Beach, Panjim, Goa. The current issue of Trans.PMAI., Vol.35, 2009 contains selected papers from this event. High strength, light weight Al-Cu-Mg alloys are used in automotive and aircraft applications. Instead of the conventional melting and casting, these materials have been processed from elemental powders by a non-equilibrium process of mechanical alloying resulting in increased solubility and improved properties. The next paper is dealt with the high energy milling process for the synthesis of multiwalled carbon nanotubes reinforced with aluminium alloy AA4032. Ultra purification of Cadmium from Indian resource for electronic applications is the subject matter of the next paper. Preparation of high purity sub-micron spheroidal Zirconia powder from impure zirconium salt through glycerol route is the award winning paper of 2009.

Hydrostatic behaviour of reaction medium on the synthesis of Zinc oxide nano particles which are promising material for optoelectronic devices and solar cells. The next three articles are dealing with powder metallurgy processing and properties of steels and stainless steels.There are also contributions dealing with lead free nano Ba-Sr-Ti ferroelectric ceramics, dry recycling of rejected mixed oxide fuel pellets for fast breader reactor and processing of aluminium AA6061-fly ash composites from elemental powders by mixing with fly ash ,pressing and extrusion. Powder Metallurgy Association of India is pleased to announce International Conference & Exhibition on Powder Metallurgy in processing of particulate materials and products & 36th.Annaual Technical Meeting during January 28-30, at Sheraton Rajputana Hotel, Jaipur.

PMAI wishes its readers a very Happy and Prosperous New Year 2010.

P.Ramakrishnan

TRANSACTIONS OF
POWDER METALLURGY ASSOCIATION OF INDIA

Vol. 35, December 2009

CONTENTS

PRODUCTION OF Al-Cu-Mg ALLOY THROUGH MECHANICAL ALLOYING -- CERTAIN OBSERVATIONS

K.Gururaj[1],Dr.G.Poshal[2]

[1]Dept.of Mechanical Engg.,KITS,Warangal.
[2] Dept of Metallurgical Engg JNT University, Kukatpally, Hyderabad.

ABSTRACT

Al-Cu-Mg alloys play a vital role in the applications where high strength – light weight materials with optimum corrosion resistance are the requirement. For example, air craft engines cylinder heads, compressor rings, piston, truck wheels, screw machine products and fittings etc., an alloy with 4.5%Cu- 1.5%Mg and 0.5% silver in 99.9% purity Aluminum is chosen. An attempt is made to alloy the powders through high energy attrition milling, and the advantage of processing route is explored. The effect of Ball to charge ratio, milling speed and milling time are presented.

The effect of Mechanical Alloying on powder characteristics is analyzed through X-ray diffraction and scanning electron microscopy. The densification and sintering characteristics are analyzed. These powders are processed through conventional P/M route and the resulting sintered compacts are studied for resulting micro structural aspects. Mechanical properties like hardness and the tensile strength are determined.

1. INTRODUCTION

Alloy development for better properties is proved to be a vital approach through synthesis of material in a non-equilibrium state consist of energize and quench as proposed by Turnbull[1]

Processes such as solid state quenching, rapid solidification, irradiation, and condensation from vapor state etc., leading to departure from equilibrium processing [2]. However, other methods of non-equilibrium processing that do not involve quenching, include static under cooling of liquid droplets, electro deposition of alloys, mechanical alloying and application of high pressures. In the present work, mechanical attrition is being chosen to develop an alloy with enhanced properties in Al-Cu-Mg alloy system with small additions of silver.

The present attempt is to develop an alloy with enhanced properties prompted by the most common grades of the alloy used for Automobile and aircraft application i.e. 2014, 2017, and 2024. A typical composition consisting of 4.5% Copper 1.5 Magnesium 0.5 % of Silver in 99.9% pure Aluminum powder. The solubility of Cu, Mg in Aluminum are around 6% and 2% respectively, under equilibrium conditions. An advantage of mechanical alloying is the enhancement of solid solubility limits in the base material. A comparison of equilibrium and extended solid solubility limits of different solute elements are indicated in Figure1.

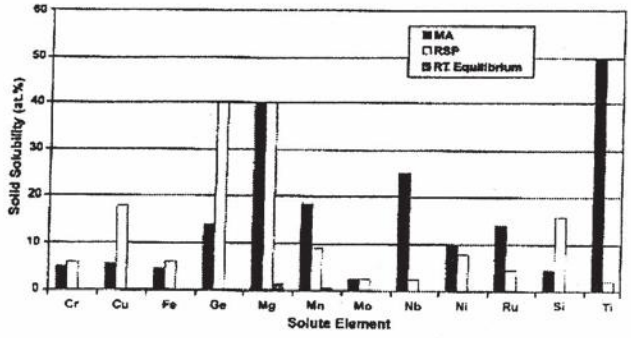

Fig.1 Comparison of room temperature equilibrium solid solubility of solute elements in Al and those obtained by mechanical alloying (MA) and rapid solidification processing (RSP).

Further, small additions of silver to the extent of around 1% is reported to increase the strength and toughness of the alloy, a desirable characteristic in most of the automobile and aircraft structures.

EXPERIMENTAL WORK:

The elemental powders are mixed in a high energy attrition mill and attrited. Specially designed and fabricated

attrition mill of 5 liters capacity is used for the present work. The height diameter ratio of the attrition vessel is 1.8:1. Hardened steel balls of balls of 10 mm and 5 mm dia are used as grinding media. Cross section of attrition mill is shown in Figure 2 and the mill in operation is shown in Figure 3. The charge was milled for 1 hour at various speeds, in argon atmosphere to prevent oxidation. The mill is maintained at ambient temperature with a coolant circulation around the mill and small addition of acetone is made to improve particle surface appearance.

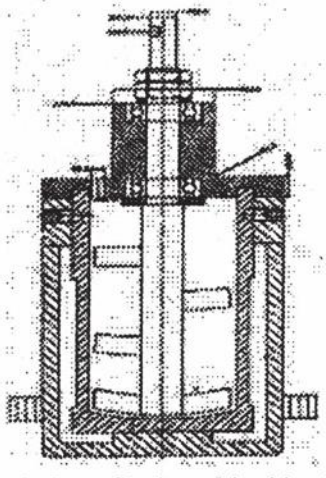

Fig . 2 Cross Section of Attrition Mill

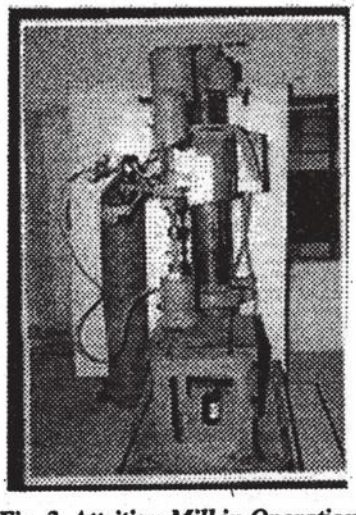

Fig 3 Attrition Mill in Operation

The size distribution of elemental powders of commercial Al, Cu, Mg before and after attrition is presented in Figure. 4.

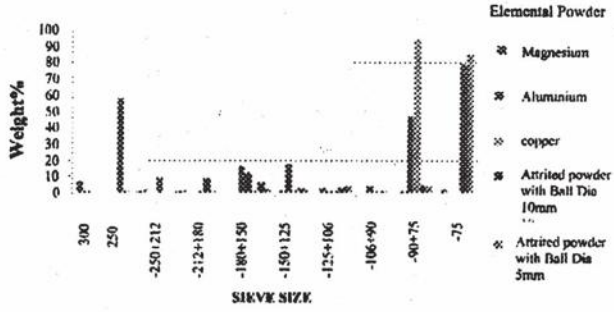

Fig 4 Histogram of the particle size distribution of the powders before & after attrition

The compressibility characteristics of the powders milled at 280 and 560 r.p.m are determined and the results are presented in Figure 5 (a) & (b)

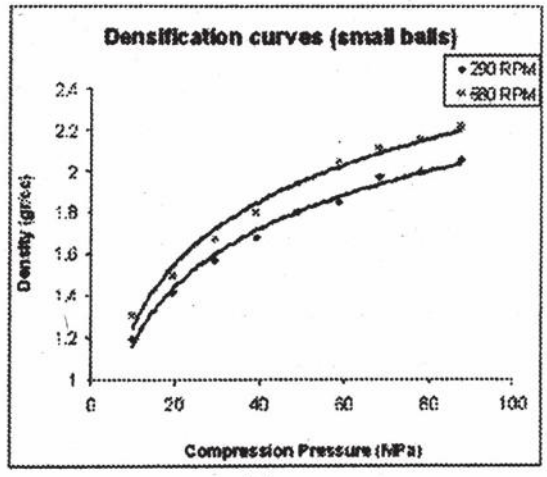

(a)

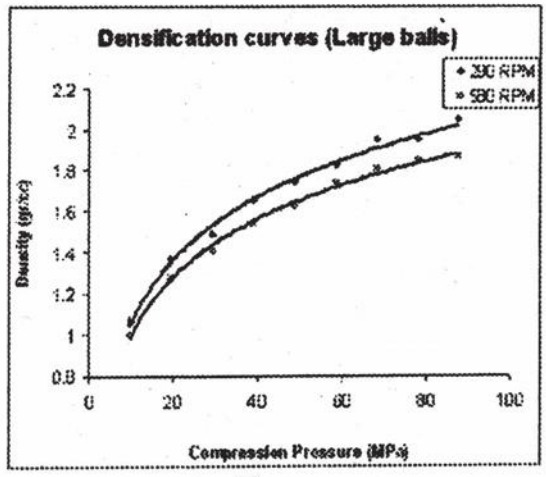

(b)

Fig. 5 compressibility characteristics of attrited powders

The surface characteristics of the attrited powders and the possibility of any compound formation in the process are analyzed by X-ray diffraction technique. Figure 6 is X-ray Diffractogram of attrition milled powders indicating Al-Cu-Mg compound formation.

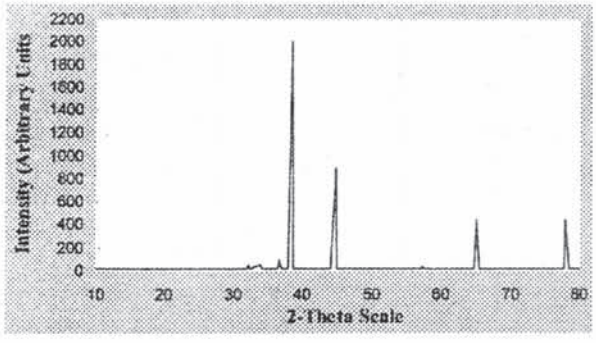

Fig 6 X-ray Diffractogram of attrition milled powder

Figure 7 presents SEM photographs of attrited powders indicating the surface characteristics. Powders thus produced are processed by conventional P/M route by dicompaction and sintered in argon atmosphere.

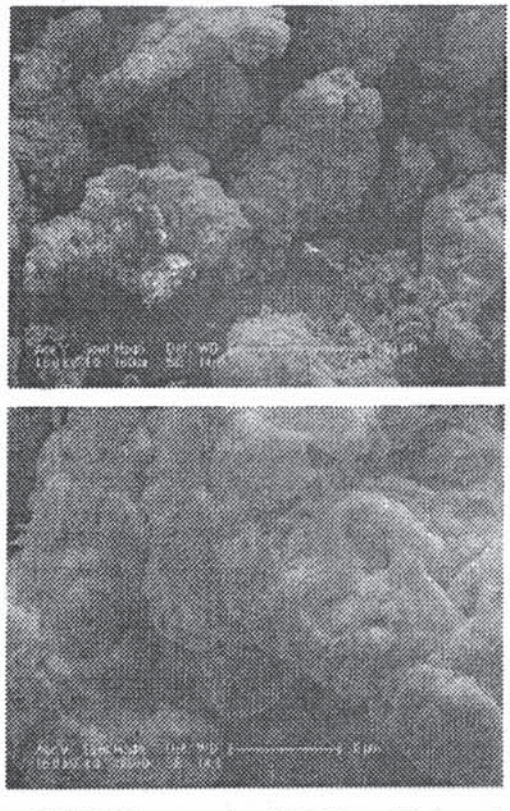

Fig 7 SEM Photographs of Attrition milled powders

Figure 8 shows the experimental setup used for compaction and Figure 9 shows the sintering setup

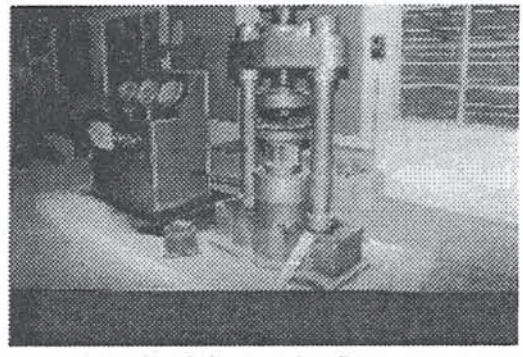

Fig. 8 Compaction Setup

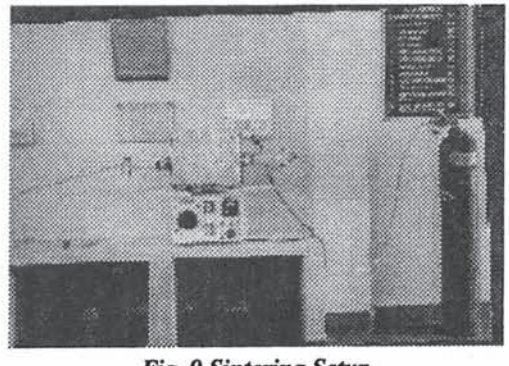

Fig. 9 Sintering Setup

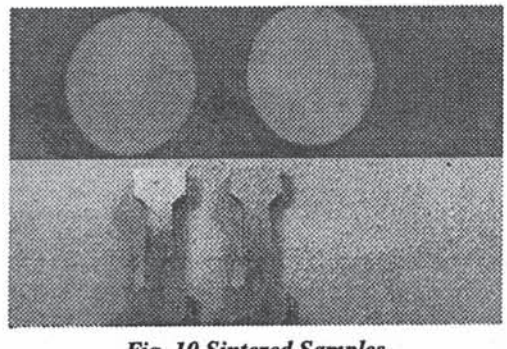

Fig. 10 Sintered Samples

Table 1 :

Hardness and Tensile Properties of Sintered Compacts

Milling Condition	V H N	Tensile Properties		
		Ultimate Tensile Strength (M Pa)	Yield Strength (M Pa)	% Elongation
5 mm Balls 290 RPM	69	53.2	45.7	15.5
5 mm Balls 580 RPM	74	58.3	51.2	13.4
10 mm Balls 290 RPM	64	49.3	42.8	14.21
10 mm Balls 580 RPM	68	54.9	48.4	14.9

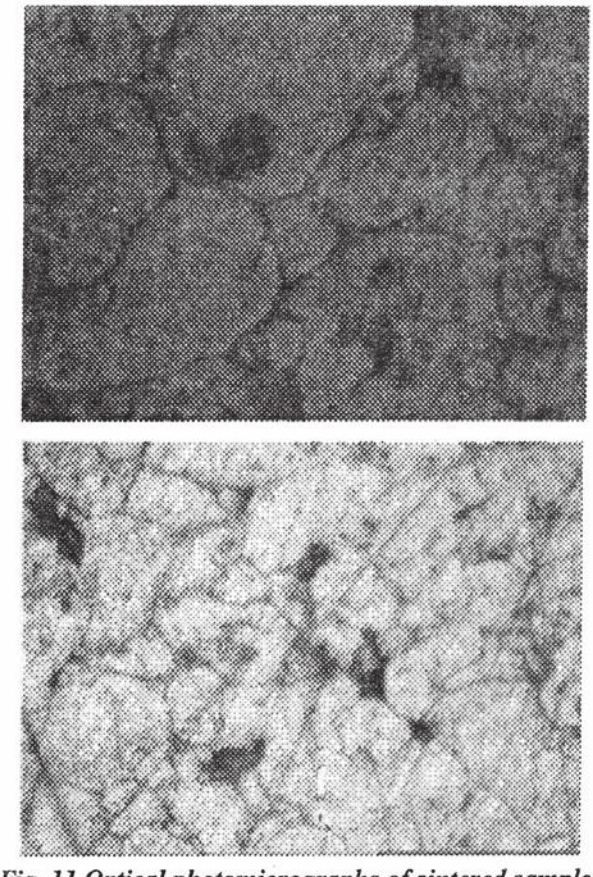

Fig. 11 Optical photomicrographs of sintered samples

RESULTS AND DISCUSSIONS:

The Attrition milled alloy powders are tested as per MPIF Standards. The results of sieve analysis are shown in Figure 4. The X-ray diffraction pattern of the milled powder indicates formation of compounds in the process. The effect of Attrition milling on the surface characteristics indicate the wavy nature of the particle surface enhancing the bonding between the particles during further processing stages. The final microstructures of compacted and sintered samples are presented in Figure 11. It can be observed from these figures that homogenous and well dispersed free micro structures could be obtained from mechanical alloying route in the alloy under study. The hardness and the tensile properties of the samples are indicate that increasing milling speed and decreasing size of the grinding media results in improved properties as presented in Table 1.

CONCLUSIONS:

The chosen composition of aluminum alloy exhibits improvement in property owing to the compound formation, and increased solubility at higher milling speeds.

ACKNOWLEDGEMENTS:

The Authors gratefully acknowledge the timely help of Shri. A. Dayanand Reddy, Managing Director, M/s. Vasantha Tool Crafts Private Limited., Hyderabad. In designing and manufacturing attrition mill with various types of shafts. Also sincerely thank The Indian Institute of Chemical Technology for their kind support in extending the facilities of Scanning electron microscope and X-ray diffraction.

REFERENCES:

1. Benjamin, J.S. (1976), Scientific American . 234(5) : 40-48
2. Turnbull, D (1981). Metall. Trans. 12A:695-708.
3. K. Gururaj and G. Sambasiva Rao "Production of missile grade magnesium powders" Trans. PMAI, Vol 18, 1991 pp 11-15.
4. Lee, P.Y., Yang, J.L. Lin, H.M. (1998) Metall. Trans. 5: 1929 – 1934.
5. C. Suryanarayana, "Mechanical Alloying and Milling" Marcel Dekker publications 2004 pg: 21 - 120, 139 – 182.

SYNTHESIS AND CHARACTERIZATION OF CNT REINFORCED Al-BASED COMPOSITE POWDERS BY HIGH ENERGY BALL MILLING

*M.S.Senthil Saravanan[a], S.P.Kumaresh Babu[a], K.Sivaprasad[a], **

[a]Advanced Materials Processing Laboratory
Department of Metallurgical and Materials Engineering,
National Institute of Technology, Tiruchirapalli.
*Corresponding author;

ABSTRACT

A few studies have focused on the preparation of metal matrix composites (MMC) reinforced with CNTs. In these composites there is evidence of poor interfacial bonding between the CNTs and the metal matrix, and this may be detrimental to the mechanical properties of these composites. Moreover, agglomeration of the CNTs may produce an uneven dispersion within the matrix which reduces their effectiveness. These are all challenges that need to be addressed in optimizing the synthesis of CNT metal matrix composites. In the present investigation, nanocrystalline AA4032 alloy reinforced with CNTs in different fractions was produced by high energy ball milling. The TEM observations revealed multi-walled CNTs that are used as reinforcement in the composite. Nanocrystalline AA4032 alloy with and without CNTs evidenced nanocrystalline matrix of the composite. TEM observations on composites revealed nanocrystalline matrix of AA4032 alloy composite along with uniform distribution of CNTs.

1. INTRODUCTION

The interest in developing new aluminium based alloys has grown largely in the past years as part of the ongoing search for new advanced materials to meet the challenges and demands for higher performance alloys. These alloys are find applications which include automotive, aerospace and many other structural applications because of their high specific strengths anand good corrosion resistance [1]. Carbon Nanotubes (CNTs) have received widespread attention in the past decade owing to their unique physical, chemical, thermal and mechanical properties [2]. CNTs are the most promising of all nanomaterials and have been studied for their potential application in storage systems, composite materials, field emission displays, nanoscale sensors, nanoscale programmable logic circuits and other electronic applications. Since CNTs possess relatively low density varying from 0.8 to 1.8 g/cc for SWNTs and 1.4 to 1.8 g/cc for MWNTs [3] the estimated high young's modulus and tensile strength of the nanotubes reinforcements make it possible use in composite materials for improved mechanical properties [4]. Nanocomposites can be processed by two rotes such as equilibrium and non equilibrium methods. Non-equilibrium methods are gas condensation, rapid solidification, and mechanical alloying. Mechanical alloying is widely used method for synthesis of nanocomposites[5]. A very limited research was done in the area of Carbon nanotubes reinforced aluminium matrix composites due to the problem of interfacial reaction between carbon nanotubes and aluminium matrices. Furthermore the CNTs reinforced aluminium alloys synthesized by mechanical milling is still very limited. In this present work, synthesis of novel aluminium based nanocomposites by combining AA 4032 alloy powders and multiwalled carbon nanotubes (MWNTs) through mechanical milling and powder metallurgy.

2. EXPERIMENTAL

Elemental powders of Al, Si, Mg, Cu and Ni (purity > 99%, 200 mesh) were used as starting materials to prepare alloys of composition given in the Table 1. MWNTs were synthesized by electric arc discharge method. The cathode is stationary one whereas the anode is moving towards the cathode. The anode was a cylindrical graphite rod (150 mm length with 10 mm diameter). The cathode was a rectangular graphite plate (size: 150 x 100 x 10 mm3). All of the experiments were carried out in open air atmosphere only. The arc was generated with a current of 150 A and 40V and the gap between the electrodes was maintained to be about 1-3 mm. The current and voltage were maintained

constant throughout the process. The graphite electrodes used were of 98.5 % purity. A TIG power source with AC/ DC inverter is used. The MWNTs produced were purified by oxidation at 600oC for 2 h, cleaned with toluene for 5 h and finally sonicated with acetone for 20 min.

The elemental powder of AA 4032 alloy was ball milled in high energy ball mill (Fritsch pulverisette P5) with Tungsten Carbide vials and balls. The ball to powder ratio was maintained as 10:1 and toluene as process control agent. The total milling time was maintained as 30 hours in all experiments so that steady state condition is reached at different compositions. The milled powders were taken at regular interval of 5h, 10h, 15h, 20h, 25h, and 30h for analysis. MWNTs at different fractions (1.0, 1.5. 2.0 wt %) were added to the AA 4032 at end of 29 h to avoid the any damage to the surface of carbon nanotubes. The phase characterization of the milled powders was carried out in XRD with Cu K radiation. The morphology of MWNTs and Al 4032 were observed by SEM (HITACHI S3000H) and HRTEM (JEOL 3010 at an excitation voltage of 200 keV).

Table: 1 Chemical composition of AA 4032 alloy

Alloying Element	Mass fraction
Sillicon	11.5
Copper	1.0
Magnesium	1.0
Nickel	1.0
Aluminium	Balance

3. RESULTS AND DISCUSSION:

3.1 X-ray diffraction Analysis

X-ray diffractions of the ball milled powders taken at regular intervals (0h, 5h, 10h, 15h, 20h, 25h, 30h) of milling are shown in fig(1). Increased broadening of -Al peaks was observed with increased milling time. This is attributed to reduction in crystallite size and increase lattice strain. Al-Aqeeli et al represented peak shift in ball milling powders, resulted in reduced grain size [6]. Similar kind of shift was observed in present investigation also, which may be attributed to variation in lattice parameter due to dissolved solute element.

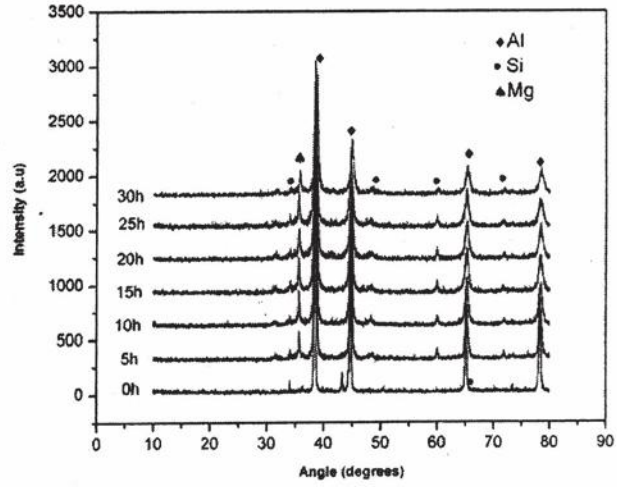

Fig 1: XRD pattern of ball milled powders taken at regular intervals of milling

3.2 Morphological Changes:

Figure (2) shows the SEM images of AA 4032 alloy powder taken at the regular intervals (0h, 5h, 10h, 15h, 20h, 25h, 30h) of milling process. The AA 4032 particles are equiaxed and irregular in shape at the initial stage. After 5 h milling, the particles deform into flake like shape due to the ductile nature of aluminum. The powder had a broad distribution of irregular particles. The alloying elements give a homogeneous mixture after 5h milling. The particles are become plate like and flattened structure after 10 h milling. The plate like particles are work hardened after 15 h milling, hence continuation of cold welding and fracture mechanism is still activated. The flake like morphology still remains after 15 h milling but the particle size decreased. After 20 h, a low aspect ratio of the powders was seen and then there is a narrow distribution in the particle size. Further milling upto 30 h, shows a uniform change in the particle size of the particles.

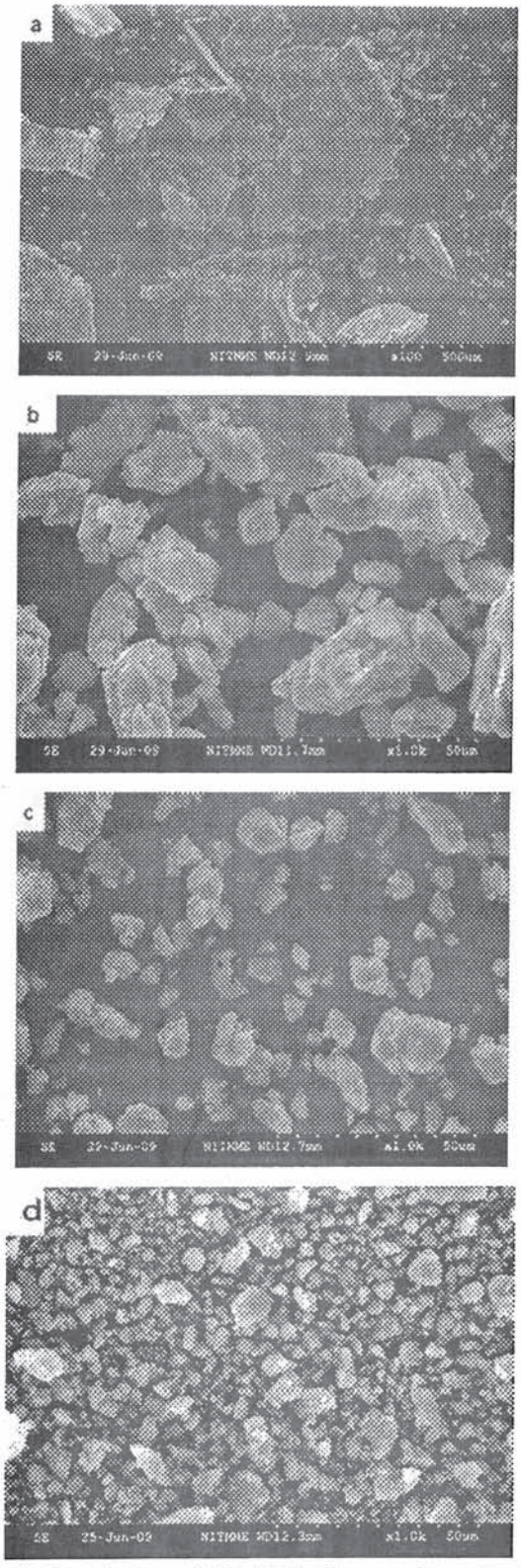

Fig 2: Morphology of AA 4032 alloy powders after (a) 0 h, (b) 5 h, (c) 10 h, (d) 30 h

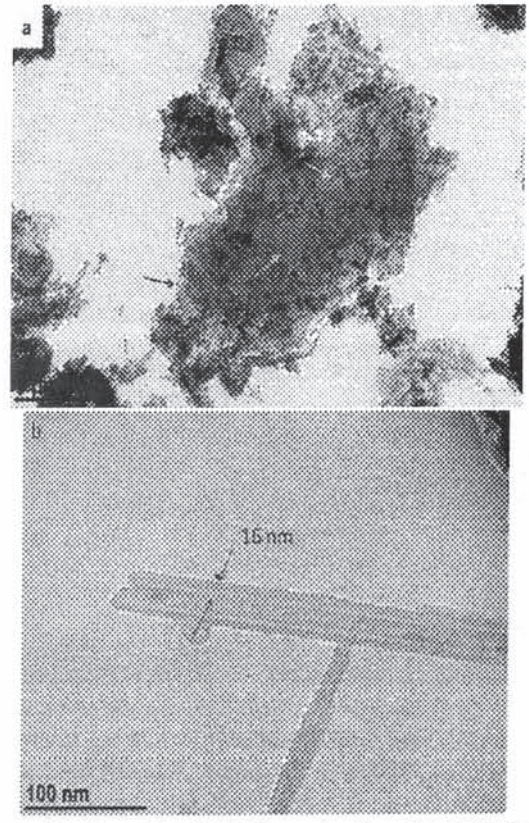

Figure(3) shows the TEM images of purified MWNTs. Fig 3. (a) Low magnification HRTEM image of MWMTs. (b) MWNTs of diameter 16nm

Figure (4a) shows bright field images of Al-2 wt % CNT nanocomposites. The MWNTs are dispersed quite homogeneously in the composite. Figure (4b) shows the corresponding selected area diffraction (SAED) pattern of AA 4032 reinforced with 2 wt % MWNTs. The obtained ring pattern in SAED evidenced the formation of nanostructured composite phase. It was found that no additional spots were formed, which confirms that no further phase was formed. In conventional Carbon/aluminium composites, Al4C3 was grown on the prismatic planes of carbon fiber. In our work, no carbides were detected at the Al/ CNT interfaces, which show a better chemical stability of MWNT. It was confirmed through the mechanical milling of Aluminium and carbon nanotube nano composites. The TEM picture shows the uniform distribution of MWNTs in the composite effectively inhibits matrix deformation and produces strengthening effect [7].

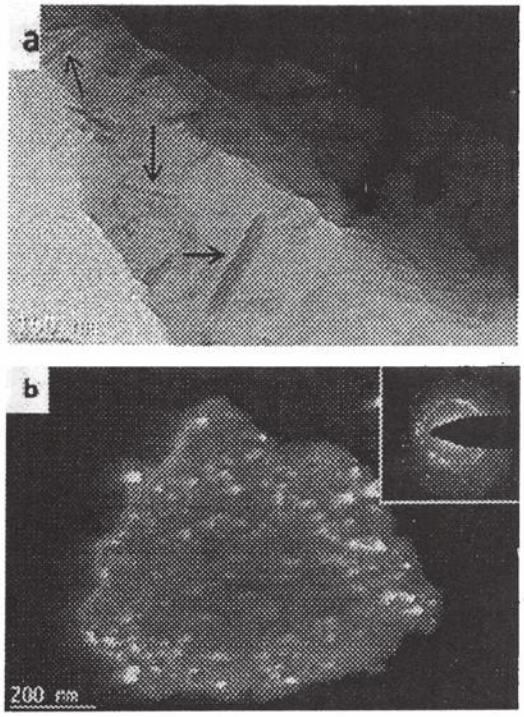

Fig 4: TEM images of AA4032 alloy reinforced with 2wt% CNTs (a) bright field image showing uniform distribution of CNTS in composite (b) dark field image of ball milled powder particle (inset corresponding SAED pattern

3.2 Particle size distribution:

Figure (5) shows grain size and lattice strain of AA 4032 alloy is plotted against milling time obtained by XRD peak broadening analysis. It shows that grain size decreases by milling time. In this work, grain size decreases rapidly in early stages and then finally it fixed as 42 nm. The lattice strain increases with increase in the milling time because of the distortion effect caused by the dislocation in the lattice.

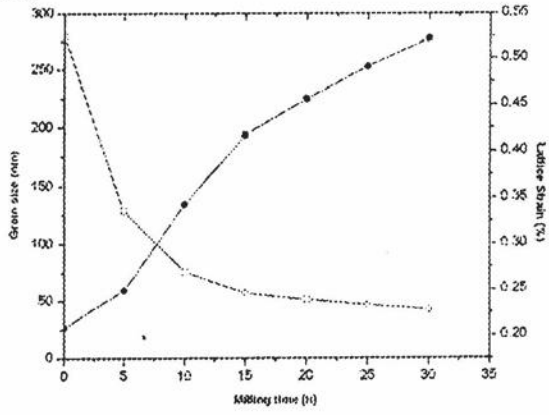

Fig 5: Grain size and strain variation with milling time

4. CONCLUSION:

Multiwalled carbon nanotubes reinforced AA 4032 alloy nanocomposites have been successfully synthesized by high energy ball milling. TEM analysis shows that MWNTs showed high mechanical and chemical stability. MWNTs were dispersed homogeneously in the Al 4032 matrix composites. Effect of milling time with grain size and lattice strain was clearly studied and there was decrease in grain size and increase in strain with increase in milling time.

REFERENCES:

1. C. Suryanarayana, E.Ivanaov, V.V. Boldyrev, The science and technology of mechanical alloying, Mater. Sci.Eng.A 304 (2001) 151
2. S.Iijima, Helical Microtubules of graphitic carbon, Nature, 354(1991) 56
3. R.George, K.T. Kashyap, R. Rahul, S. Yamdagni , strengthening in Aluminium/CNT Composites, Scripta Materialia 53(2005) 1159
4. G. Overney, W. Zhong, and D. Tománek, Structural Rigidity and Low Frequency Vibrational Modes of Long Carbon Tubules, Z. Phys. D 27, (1993) 93.
5. D.L.Zhang, Processing of advanced materials using high energy ball milling Prog.Mater.Sci. 49(2004) 537
6. N.Al-Aqeeli, G.Mendoza saurez, C.suryanarayana , R.A.L . Drew, Development of new Al-based nanocomposites by mechanical milling, Mater.Sci. Engg A 480(2008) 392
7. R.Perez-Bustamante, I.E. Guel, W.A. Flores, M.M.Yoshida, P.J.Ferreira, R.M.Sanchez,, Novel Al-Matrix nanocomposies reinforced with multi walled carbon nanotubes, J.Alloys and Compounds 450(2008) 323

ULTRA PURIFICATION OF CADMIUM FROM INDIAN RESOURCE: SOME STUDIES

D. S. Prasad, N. R. Munirathnam*, N. Murali Babu and T. L. Prakash*

Centre for Materials for Electronics Technology (C-MET). Hyderabad.

ABSTRACT

The prime objective of the study is to purify cadmium from indigenous source for optoelectronic applications which is accomplished by adopting complimentary technique, comprising of selective vapourization and horizontal zone refining. The average content of impurity elements of raw cadmium (3N pure) was reduced to the extent of achieving 5N+ pure by selective vapourization process under a dynamic vacuum of 6 x 10-4 torr. An average distillation rate of 2.1 x 10-4 g cm-2 sec-1 was obtained at 400 0C of distillation temperature. In the second approach, zone refining process has been adopted to achieve ultra high pure cadmium. A detailed discussion on the quantitative reduction of crucial impurities is presented in this study.

1. INTRODUCTION

The study of materials in a high state of purity has become a subject of vital interest and where unique properties have been shown to be associated with high purity, it has been necessary to consider development and production of those materials. CdTe based polycrystalline thin film solar cells have been considered as one of the most promising candidates for large scale, cost effective, terrestrial photovoltaic applications. Ultra pure cadmium has become one of the important metals in fabricating CdTe/ CdZnTe compound semiconductors used mostly in the strategic sector for fabricating high performance infrared (IR) devices. The background levels of electrically active impurities for IR applications should be in the range of 0.3 – 15 ppb in mercury cadmium telluride (MCT) devices [1].

Cadmium is one of the most difficult metals to zone refine because of its low melting point and high thermal conductivity [2]. There are several purification methods established to obtain 6N and above purity cadmium starting with a gross approach followed by more refined purification steps. The non-chemical routes usually followed to purify cadmium are vacuum distillation followed by horizontal zone refining [3]. In addition to the process methodology, the quality of the output material depends on the impurity content of the input material. The scientific information of separation of impurities from the two processes such as vacuum distillation and zone refining is important in developing viable pilot plant scale technologies.

EXPERIMENT

The process flow sheet for cadmium purification is shown in fig. 1. The cadmium of 3N purity available from local market was purchased and cleaned using dilute acids and nano pure water. Vacuum distillation was carried out in the first step followed by multiple zone refining to achieve high pure cadmium. The vacuum distillation experiment was conducted in two phases. In the first phase, called as first fraction stage, the distillation experiment was carried out at 350^{0}C to remove high vapour pressure impurities. There after, the "first fraction" material was removed and then the balance material was used in the second phase, called "middle fraction" (main distillation). Distillation temperature of about 400^{0}C was maintained. Samples of condensate were collected at time intervals of 30 minutes in the case of first fraction experiment and 4h in the case of middle fraction experiment, after the melt has attained the respective distillation temperature. The purification yield was found to be in the range 75 – 95%. In a similar

approach, second and third stage distillations were carried out. After each distillation, the sample for analysis was taken from the distillate by random selection and mixing at four to five places in order to obtain an average impurity concentration. The elemental impurities in cadmium were analyzed by ICP-OES and ICP-MS.

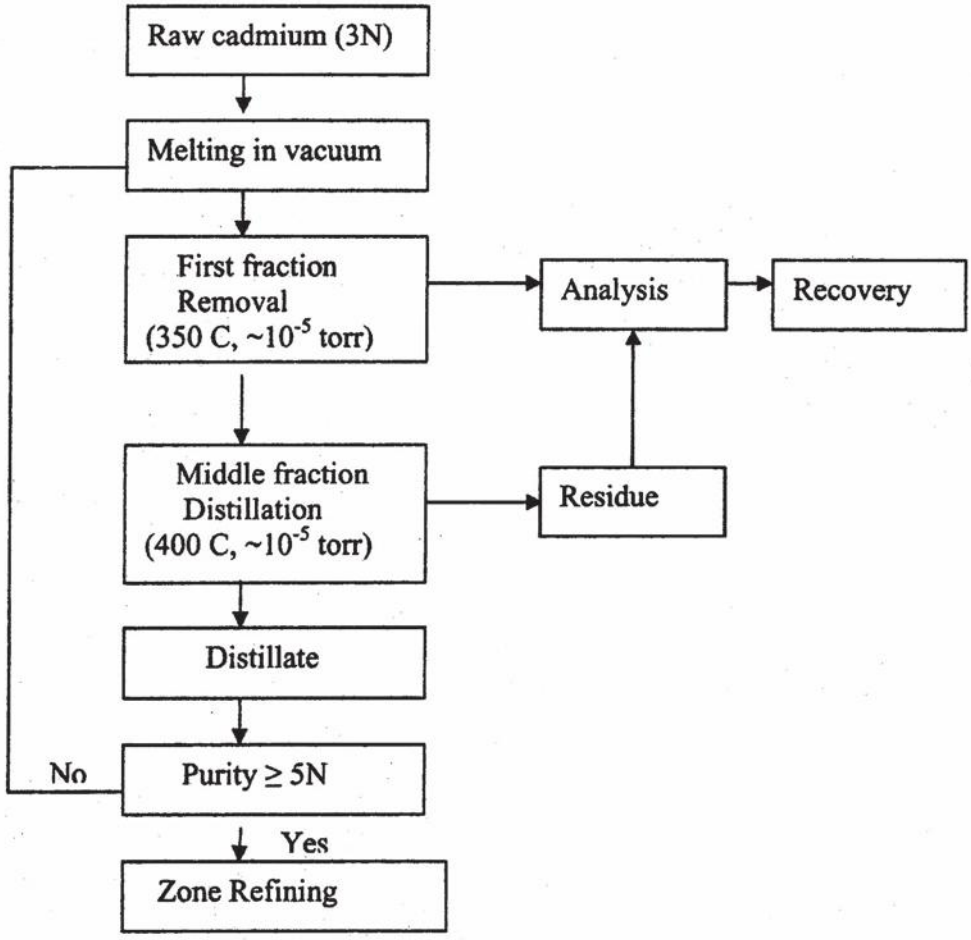

Fig. 1: Process flow sheet of cadmium purification

The vacuum distilled cadmium was uniformly melted to make an ingot of ~560 mm length at ~400°C in pre-evacuated tube (1x10-2 torr) under hydrogen atmosphere with a flow rate of 100 to 200 SCCM and then cooled. Inert gas purging was continued until room temperature was reached. Samples from the ingot were cut and analysed by ICP-OES to determine the initial concentration of impurities. The cadmium prepared in the shape of a uniform semi-circular bar was loaded into a thoroughly etched and cleaned pyrolytic coated quartz (GE 214 grade) boat of 34 mm x 38 mm x 17 mm (ID x OD x Ht.) and inserted into a cleaned 44 mm dia and 1600 mm long quartz tube. An automated microprocessor based horizontal zone refiner was used for zone refining operation. The microprocessor was programmed for 15 passes (1 cycle). After first cycle of zone refining, in order to further purify the material, the ends of the cadmium bar of approximately one zone length were chopped off. The middle portion of the bar was again melted to distribute the impurities uniformly in the entire ingot length and then second set of 15 zone passes were completed. The speed of the stepper motor was set at 3cm/h during zone refining experiment and in this mode two cycles, which is 30 passes were carried out. At the end of each cycle, the zone-refined ingot was cut into three portions, viz. right end portion, middle portion and left end portion. The sample from middle portion was analyzed to determine impurity concentration.

RESULTS AND DISCUSSION

The impurity content in the starting material, vacuum distilled and zone refined cadmium are given in table-1. It is observed that most of the impurities except Zn were considerably reduced after third distillation. Gradual reduction of major impurities was observed on subsequent distillation. The residue left at the evaporator contained major impurities such as Fe, Ni, Cu, Ag and Bi. The concentration of Zn was slightly reduced during first fraction experiment due to its high vapour pressure and indicates that "first fraction" need to be removed before distillation experiment. The average distillation rate was found to be 2.1 x 10-4 g cm-2 sec-1 and observed that the rate of deposition is a function of time. It is seen from the analytical data that the distillate material (middle fraction) contains less content of Pb, Bi, Ni, Fe, Cu, Cr, Mn, Mg, Ag, etc. were reduced to the extent of ppb level only after subjecting to three consecutive distillations.

Table 1
Analytical data of purified cadmium

(All values are in ppb)

S.NO	Impurity Elements	Input	Vacuum Distilled material	Zone refined material
1	Cr	100	27.5	15
2	Zn	11000	3500	850
3	Pb	460000	750	4.2
4	Bi	1000	200	55
5	Co	1000	30	10
6	Ni	11000	150	25
7	Fe	100	40	110
8	Mn	100	22	4
9	Mg	100	10	3
10	Cu	37000	650	15
11	Ag	18000	10	21
12	Al	1000	8	1.0
13	Ca	1000	6	1.0
14	As	1000	10	<10

The segregation behaviour of impurities namely, Cr, Zn, Pb, Bi, Co, Ni, Fe, Mn, Mg, Cu, Ag, Al, Ca and As was studied after subjecting cadmium to 30 multiple zone passes. Removal of impurities in a material during zone refining depends on the distribution coefficient (K) of a particular impurity as also the initial impurity content [4]. The 'K' value of many of the impurities except Ag, Mg in cadmium is less than one and therefore they were segregated to tail end where as Ag and Mg whose 'K" value is >1 moved towards starting end. The initial concentration of Pb, Ni, Cu is slightly higher and were reduced to the extent of only 4.2, 25, 15 ppb respectively after two cycle (30 passes) of zone refining operation which indicates that the reduction of concentration of impurities during zone refining is dependent not only on the value of distribution coefficient but also on the initial content. It was also noticed from the results that the crucial impurity namely, Zn was decreased up to 850 ppb from 11000 ppb implies that the impurity, Zn which is very difficult to remove by vacuum distillation can be reduced by zone refining but requires large number of zone passes as its "K" value is higher (0.4). Also, it can be said that the concentration of other impurities such as Cr, Bi, Co, Fe, Cu and Ag in addition to Zn will be further reduced by increasing the number of zone passes which is a scope for further study.

CONCLUSION

- By combination of selective vaporization and zone refining 3N pure cadmium was purified up to ultra high pure grade (6N) for opto electronic applications.

- The crucial high vapour pressure impurity "Zn" was reduced in first fraction during vacuum distillation process and further reduced by zone refining process.
- The zone travel rate of 3cm/h yield better results and significant degree of separation of impurities was achieved. The segregation of impurities during zone refining were influenced by initial concentration as also on the value of distribution coefficient.

REFERENCES

1. Capper. P and Harris, J.E, The bulletin of Selenium – Tellurium, 1997
2. Bult. R.P, Bollong. A.B.I and Redden. R.F, US patent no.4690725, 1985.
3. Kuchar. L, Drapala. J, Lunacek. J, J. Crystal Growth, 161, 1996, p. 94
4. Feldewerth. Gerald B, Spokane, Bollong. Alan B. I, Veradale, Bunnell. David C; US Patent No. 5,513,834, 1996

PREPARATION OF HIGH PURITY SUB-MICRON SPHEROIDAL ZIRCONIA POWDER FROM IMPURE ZIRCONIUM SALT THROUGH GLYCEROL ROUTE

Amit Sinha[1], P. K. Sinha and B. P. Sharma

Bhabha Atomic Research Centre, Navi Mumbai.

ABSTRACT

Using a simple energy efficient process, high purity fine zirconia powder with uniform particle morphology was prepared starting from impure zirconyl chloride. The process involves hydrolysis of zirconium in glycerol media and subsequent removal of impurity elements by controlling the process parameters. Glycerol, in this process, acts as a solvent as well as a reducing agent. The zirconia powders prepared through this process were characterized by X-ray diffraction (XRD), scanning electron microscopy (SEM), BET surface area analysis, thermo-gravimetric analysis and chemical analysis. The zirconia powder produced through this process was having a purity greater than 99.9 %.

1. INTRODUCTION

Pure zirconia (ZrO_2) is one of the major constituents of ceramic colors and an important component of lead zirconia titanate based electronic ceramics. Pure zirconia is monoclinic (m) at room temperature. During heating, m-ZrO_2 t-ZrO_2 (tetragonal) and t-ZrO_2 cZrO_2 (cubic) phase transformations take place at 1170 and 2370 °C respectively. The cubic phase is stable up to the melting point (2680 °C) of zirconia. The t-ZrO_2 m-ZrO_2 phase transformation is accompanied by a large volume change (3-5%) leading to disintegration of the ceramic body during cooling from the sintering temperature and subsequent application. However, addition of aliovalent oxide additives i.e. CaO, MgO, or Y_2O_3 into the zirconia stabilizes the high temperature cubic phase through the formation of vacancy at oxygen sublattice. The cubic zirconia is used in grinding media and engineering ceramics due to its increased hardness and high thermal shock resistance. It is also used in applications such as oxygen sensors and solid oxide fuel cells due to its high oxygen ion conductivity. Preparation of pure zirconia is usually carried out starting from zircon ($ZrSiO_4$). In this process, the first step is to convert zircon to zirconyl chloride. It can be done through the following chemical reactions:

$ZrSiO_4 + 4NaOH$, $Na2ZrO_3+Na2SiO_3+2H_2O$ (1)

$Na_2ZrO_3 + HCl$, ZrOCl2. 8H2O (2)

For the preparation of zirconia powder from zirconyl oxychloride, there are basically two methods, e.g. thermal decomposition and precipitation. In thermal decomposition, once $ZrOCl_2$. $8H_2O$ is heated to 200°C it starts dehydrating and becomes anhydrous $ZrOCl_2$ which on subsequent heating forms zirconia. This method is associated with low production cost. The limitations of this process include large impurity content in powder as well as difficulty in producing powder with fine particle size. Precipitation method, on the other hand, uses chemical reaction to obtain zirconium hydroxide as an intermediate which forms zirconia powder on subsequent calcination.

The application of advanced ceramics in structural and electrochemical applications calls for a fine, uniform microstructure along with very high sintered density. This in turn calls for oxide powders with outstanding characteristics in terms of particle morphology, composition and purity. One of the promising routes for synthesis of high-quality ultrafine ceramic powders is wet-chemical method [1]. For the preparation of ceramic powders through precipitation from a liquid starting salt, solvents such as polyols offer two advantages: the high dielectric constants of polyols

facilitates dissolution of inorganic compounds and their high boiling point offer a wide operating temperature range (room temperature to boiling point) that permits hydrous reaction that cannot be possible in aqueous solution under atmospheric pressure. These potentials of polyols have been greatly exploited for preparation of metal powders with controlled morphology [2, 3].

There have been a few reports on the preparation of ceramic powders using polyol medium. Matijevis and Climas prepared uniform colloidal iron (III) oxide in water – ethylene glycol solution [4]. Typical processes that utilize inorganic salts as precursors for solution-synthesis of oxide ceramic powders include forced hydrolysis or other hydrothermal processing, that usually calls for relatively high temperatures to induce hydrolytic reactions, condensation, and the subsequent formation of oxide particles. As kinetics of the forced hydrolysis process is relatively slow, one of the strategies to enhance the particle formation kinetics is to add a low dielectric medium to the aqueous solutions of inorganic salts. Controlling the dielectric property of the mixed alcohol–water solvent influences not only the solubility of the dissolved solute but also the colloidal interaction between solid particles.

In the present article, we report the preparation of high purity nanocrystalline spheroidal zirconia powder from impure zirconyl chloride salt using a polyol process. The same process has also been utilized for preparation of yttria stabilized zirconia powder.

2. EXPERIMENTAL

Impure zirconyl chloride ($ZrOCl_2$) containing 1 wt % iron impurity (Indian Rare Earth, India) was used as starting material for the preparation of zirconia powder. A predetermined amount of starting salt was mixed with glycerol (AR grade). The mixed solution was heated, while stirring, on a laboratory hot plate. The reaction temperature was measured using a thermometer submerged into the solution through a glass port. After the precipitation of precursor powder, the suspension obtained was naturally cooled to room temperature and then diluted with ethanol. The Zr-containing precipitates were recovered from the suspension by repeated centrifugation followed by washing with ethanol. The powder obtained was dried under vacuum at 120 °C for 1 h. Decomposition behavior of Zr+4 precursor was studied by thermo-gravimetric analyzer up to a temperature of 800 °C under flowing air atmosphere at a heating rate of 10 °C / min. Based on the thermal analysis data, the precursor was calcined at 650 °C for 2h. The phase analysis of the dried precipitate as well as the calcined powder was carried out by X-ray diffraction using CuK. radiation at a scanning rate of 0.05 °/sec. The specific surface area of the powder was measured by conventional nitrogen BET surface area analyzer. The morphology of the calcined powder was studied by scanning electron microscope.

For preparation of 8 mol% yttria stabilized zirconia (YSZ) powder, $Y(NO_3)_3$ was used as starting material along with $ZrOCl_2$. The precursor powder obtained from the process was calcined at 700 °C for 1 h to form the desired phase. The phase analysis of the calcined powder was carried out using room temperature. To study the evolution of phases as a function of temperature and also to study the crystal growth behavior of the calcined powder at different temperatures, high temperature XRD study was conducted on calcined powders.

3. RESULTS AND DISCUSSION

3.1 Preparation of pure Zirconia powder The flow sheet of preparation of zirconia powder through glycerol route is shown in Fig. 1. When a zirconyl oxychloride solution with an alcohol-water mixture as a solvent is heated, the dielectric constant of the solution decreases significantly with increase in temperature leading to super-saturation of salt solution and subsequent precipitation [5]. In the present investigation, it was observed that Zr+4 started to hydrolyze and precipitate out of the solution at 140 °C. The TG curve for zirconium precursor, as shown in Fig 2, shows that decomposition is complete below 550 °C. Based on the thermal analysis data, the precursor was calcined at 650 °C for 2 h. The XRD pattern of the calcined precursor is shown in Fig. 3. The pattern exhibits the diffraction peaks corresponding to of tetragonal and monoclinic phases of ZrO_2.

The SEM photomicrograph of the zirconia powder produced through this route is shown in Fig. 4. The micrograph reveals that the powder is spheroidal having narrow size distribution. The crystallite size calculated from X-ray line broadening using the Scherreer formula was 12 nm. The BET specific surface area of the powder is 48 m2/gm which corresponds to a crystallite size of 20 nm. The chemical analysis of the powder indicated that it contained less than 100 ppm of iron and purity of the zirconia powder was greater than 99.9 % .

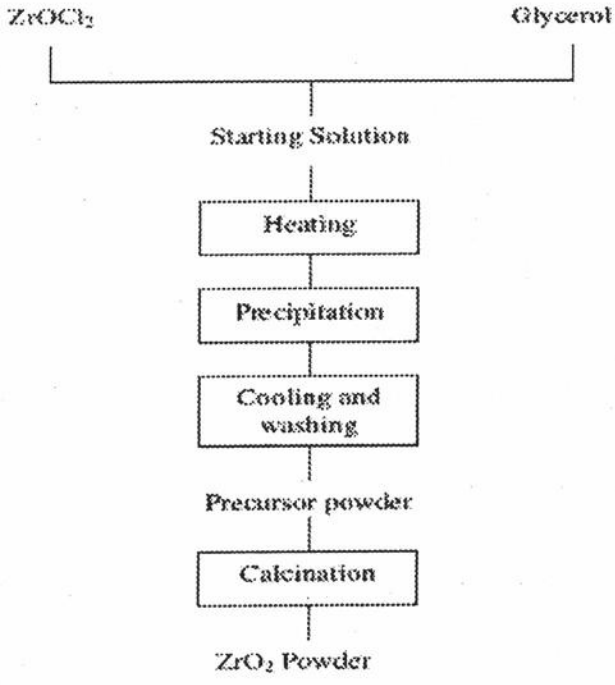

Fig 1: Flow Sheet of preparation of zirconia powder through glycerol route

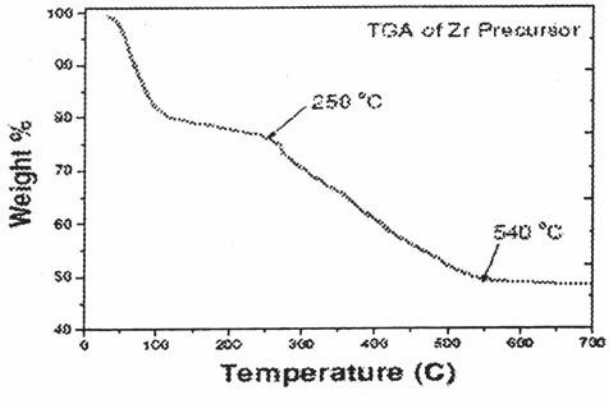

Fig 2: TG plot of Zr containing precursor obtained through glycerol route.

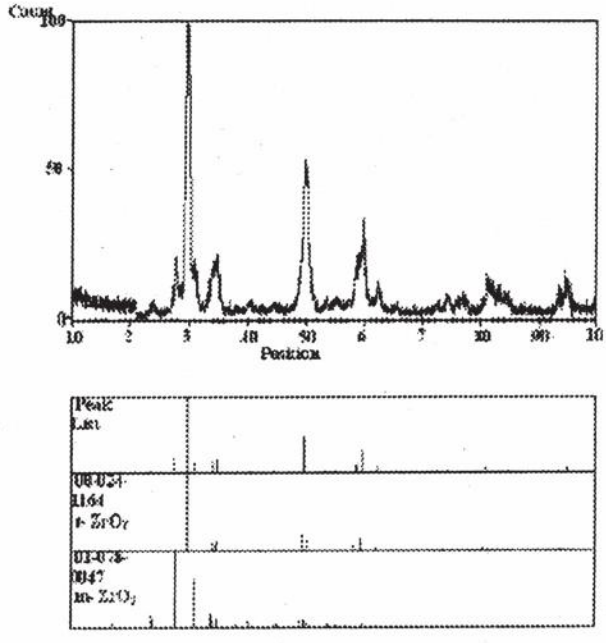

Fig 3: XRD Pattern of Zr-containing precursor calcined of 650°C for 2h.

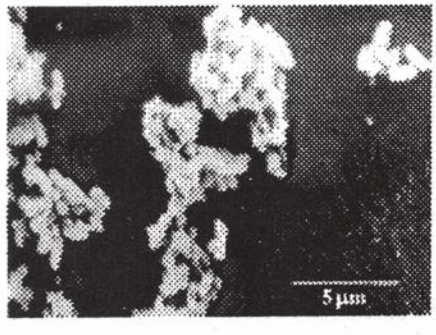

Fig 4: SEM Photomicrograph of zirconia powder calcined at 650°C for 2h.

The above results suggest that powder produced through this route exhibit a very high purity and a good crystallinity. The particles have a regular and polyhedric shape i.e. their growth is isotropic.

3.2 Preparation of yttria stabilized zirconia

The XRD pattern of YSZ powder prepared through glycerol route which was calcined at 700 °C for 1 h, is shown in Fig. 5. The pattern exhibits all the peaks corresponding to cubic polymorph of zirconia. The crystallite size of the calcined powder was calculated from the line broadening of the strongest XRD reflection. To calculate the crystallite size of the powder as a function of temperature, the XRD patterns were recorded in the temperature range of 700 to 1000 °C. The average crystallite size of the YSZ powder heated to different temperatures was determined from

the line broadening observed for the peak corresponding to the (101) reflection using the Scherrer's formula. The YSZ powder was found to be nanocrystalline having a crystallite size of 6.8 nm at 700 °C and 10 nm at 1000 °C. It was observed that the calcination temperature has greater influence on final crystallite size than calcination time.

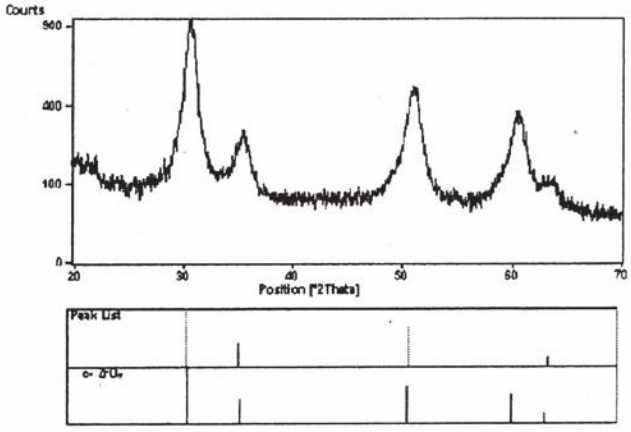

Fig 5: XRD pattern of YSZ powder calcined at 700°C for 1h.

4. CONCLUSIONS

A simple energy efficient process has been described for preparation of zirconia powder starting from impure $ZrOCl_2$ as a precursor for zirconia. It essentially consists of dissolving the zirconia precursor in glycerol followed by hydrolysis and precipitation from the solution. The process yields nano-crystallized zirconia powder having a purity greater than 99.9 %.The XRD analysis of the powder calcined at 650 °C indicates the presence of tetragonal polymorph of zirconia. The same process was also utilized for preparation of YSZ powder which yields nanocrystalline cubic ZrO_2 when the precursor powder was calcined at 700°C.

REFERENCES

1. Amit Sinha, and B. P. Sharma, "Novel Route for Preparation of High Voltage Varistor Powder", Materials Research Bulletin, Vol. 32 (11) pp. 1571-1579 (1997).
2. Amit Sinha, and B. P. Sharma, "Preparation of silver powder through glycerol route", Bulletin of Materials Science Vol. 28 (3), pp 213 – 217 (2005)
3. Amit Sinha, and B. P. Sharma, "Preparation of copper powder by glycerol process", Materials Research Bulletin, Vol. 37 pp. 407-416 (2002).
4. H. Matijevis and S. Climas, "Formation of uniform colloidal iron (III) oxides in ethylene glycol-water solutions", Colloid Polym. Sci., Vol. 265 pp. 155 -163 (1987).
5. O. Madelung, "Numerical Data and Functional Relationships in Science and Technology", Landolt-Börnstein New Series IV/6, Springer-Verlag, NY 1996.

HYDROSTATIC BEHAVIOUR OF REACTION MEDIUM ON THE SYNTHESIS OF ZINC OXIDE NANO PARTICLES

S. P. Ansari[1], A. H. Ansari[2] and F. Mohammad[1]*

1Department of Applied Chemistry,2Mechanical Engineering Section
Aligarh Muslim University, Aligarh.

ABSTRACT

Fine powders of zinc oxide are conventionally used in paint formulations, cosmetics, catalysis and gas sensors. It is a promising material for optoelectronic devices also, for example, light emitting diodes, flat display screens and solar cells due to its wide band gap. These applications require well defined crystals; therefore, the significance of its synthesis and characterization has increased incredibly in the recent years.

Numerous chemical strategies have been reported to synthesize micro and nano scale zinc oxide particles. Solvent based process is the efficient and simple technique to synthesize well defined crystals of zinc oxide. In the present paper, the effect of buoyancy offered by the solution in the growth of zinc oxide crystals is studied. Zinc acetate dihydrate and sodium hydroxide are used to synthesize zinc oxide crystals.

It was observed that buoyancy favors the growth of the zinc oxide crystals to a certain limit. Thus produced zinc oxide particles were characterized by FTIR and SEM. Mechanism of the growth of zinc oxide crystals favored by the buoyancy of solution is also discussed. The N-Cetyl-N,N,N-Trimethylammonium Bromide (CTAB) was observed to favor the directional growth of the crystals.

1. INTRODUCTION

Research in the field of nano sized materials has increased enormously during past some years. Nanomaterials is an exciting field, both for the fundamental study and the applied research. The novel optical, electrical and mechanical properties of devices comprising nanocrystalline semiconductors and oxides have been demonstrated in photovoltaic solar cells, light emitting diodes, electrochromic devices etc.

There has been a great deal of interest in zinc oxide owing to its piezoelectric properties and band gap in near ultraviolet region (Eg=3.37 eV and excitation binding energy of 60 meV) and thus has many industrial applications. Zinc oxide is a technologically important material because it produces an efficient blue-green luminescence and displays an excitonic ultraviolet (UV) laser action at room temperature1-3. It is one of the few oxides that show quantum confinement effects in experimentally accessible particle size range. In nanoparticles of zinc oxide, the nanosize particles lead to a great increase in the surface area. Larger surface area means greater number of surface defects that play an important role in controlling the surface properties as the electronic processes are strongly influenced by surface properties. Nanoparticles of zinc oxide are the one of the multifunctional inorganic nanoparticles that possess many significant physical and chemical properties such as chemical stability, low dielectric constant, large electromechanical coupling coefficient, high luminous transmittance, high catalytic activity, intrinsic ultraviolet and infrared absorption etc. As a result, zinc oxide nanoparticles can be used as/in catalysts, gas sensors, field emission displays, piezoelectric devices, UV shielding materials etc. Zinc oxide nanoparticles have high sensitivity even at room temperature whereas thin film gas sensors often operate at elevated temperatures. Recently, zinc oxide has been used in dye sensitized solar cells as an electrode material[4-6].

There are numerous ways of producing zinc oxide particles of various sizes and the process conditions vary from high temperature (above 1000°C) and high pressure (above atmospheric pressure) to low temperature and atmospheric pressure. The production of zinc oxide nanoparticles by reported methods requires sophisticated equipments and the reaction time is also significantly longer. The technique proposed by Ansari et. al.13 involves atmospheric pressure

and low temperature (below the boiling point of water) as well as it does not require any sophisticated equipments for the production of zinc oxide nanoparticles.

EXPERIMENTAL

Zinc acetate dihydrate, sodium hydroxide, N-cetyl-N,N,N-trimethylammonium bromide (CTAB) were purchased from CDH, India. All the chemicals were used as received without any further purification. Stock solutions of zinc acetate dihydrate [0.1M] (solution-A), sodium hydroxide [2M] (solution-B)7, CTAB8 [0.1 M] were prepared in double distilled water. 90 ml of double distilled water was taken in a conical flask and 5 ml of solution-A was added to it, followed by the addition of 5 ml of solution-B. The mixture was heated to 70°C with vigorous stirring for 15 min and then kept undisturbed for a determined period of time. The reaction was carried in absence CTAB as well as in presence of CTAB for its different concentrations. The precipitates were separated, washed with double distilled water and acetone and then dried for 1hr.

RESULTS AND DISCUSSION

It is well known that elongated hexagonal zinc oxide crystals grow along the c-axis and has both the polar and non-polar surfaces. The non-polar crystal faces are more energy favorable and hence more stable than those that are polar.

In solution, growth units could deposit on to zinc oxide nanoparticles from all the directions and stacked on each crystal face. The reaction intermediates decompose into zinc oxide nanoparticles as the reaction proceeds and serve as seedling for the further deposition leading to the growth of the particles9.

There is an important distinction to be made between aqueous solution deposition of zinc oxide (thin film/ precipitate) from open and closed baths, the latter conditions lead to the hydrothermal process. In general, the solubility of zinc oxide is greater under hydrothermal conditions and thus growth is typically slower10. In the present paper, the effect of reaction medium on the formation of zinc oxide nanoparticles is studied while the water is used as the reaction medium.

In our experiment, when the concentrations of Zn^{++} and OH^- reach the supersaturation, zinc oxide nuclei are formed according to the following equation.

$$(CH_3COO)_2Zn + 2\ NaOH \rightarrow ZnO + H_2O + 2\ CH_3COONa$$

In solution phase synthesis, processes like coarsening and aggregation can compete with nucleation and growth of the nanoparticles and play a crucial role in modifying the particle size distribution in the system. According to Lifshtiz-Slyozov-Wagner model, the rate of coarsening is given by the equation:

$$(r)^3 - (r_o)^3 = kt$$

where r is the average particle radius, (ro) is the initial particle radius, "t" is the time and "k" is the rate constant. The rate constant is dependent on the molar volume of the solid phase, the surface energy, the bulk solubility and the diffusion coefficient for metal ions in the solution11.

Fig. 1 shows the FTIR spectrum of the zinc oxide particles prepared by this process. The absorption peak at 1589 cm-1and 1408 cm-1 are assigned to surface adsorbed carboxylate anions which are chemisorbed on surface of the zinc oxide particles. The peak at 480 cm-1 is assigned to Zn-O bond. The bands observed at 905 and 3378 cm-1 are associated with characteristic vibrations of –OH group adsorbed on the surface of the zinc oxide particles12.

The morphology of thus prepared zinc oxide particles was characterized by SEM and the typical images are shown in Fig. 2(i)-(iii). It was observed that when solution was given sufficient time (24 hrs), the particles grew and settled down at the base of the flask. It was due to the fact that the weight of the particles exceeded the buoyancy of the solution. For floating bodies, the weight of the body should be less than the buoyancy of the fluid. The particles were separated through filtration process. However, when the time for coarsening was reduced to a maximum of 0.5 hrs, the hazing of the reaction mixture got reduced but the settlement of some particles was observed. TABLE-1 gives a detailed idea of preparation parameters at a glance.

TABLE.1. Preparation parameters of zinc oxide nanoparticles.

Reference	Reaction Medium	Growth Period	Shape Size	Particle
Fig.2 (i)	Water	24 hrs	Flowerlike	300-500 nm
Fig.2 (ii)	Water	0.5 hrs	Flowerlike	180-300 nm
Fig.2 (iii)	Aqueous CTAB (0.01M)	24 hrs	Rod	Dia~200-300 nm

This indicates that few particles undergo coarsening and settle down because of their larger size by overcoming the buoyant force of the reaction mixture. But during the shorter period experiment, a good number of particles remained suspended in the solution because of their small size. When the growth period was reduced to much short (~1-2 min.), no particle settlement was observed. Such particles could not be separated by filtration. It infers that smaller particles, more precisely particle in nanometer

domain, could not overcome the buoyancy of reaction mixture and remained suspended in the solution. These smaller particles were separated by centrifuge. We have discussed this forced separation of particles in our second communication.

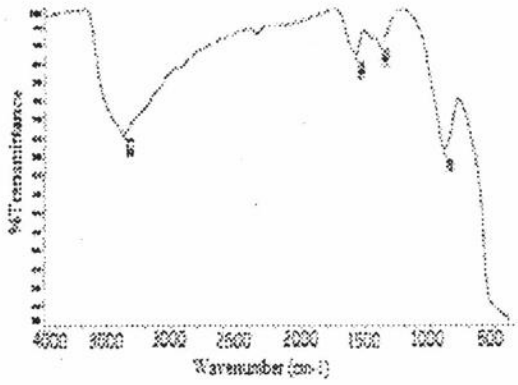

Fig. 1 FTIR spectrum of zinc oxide prepared without surfactant.

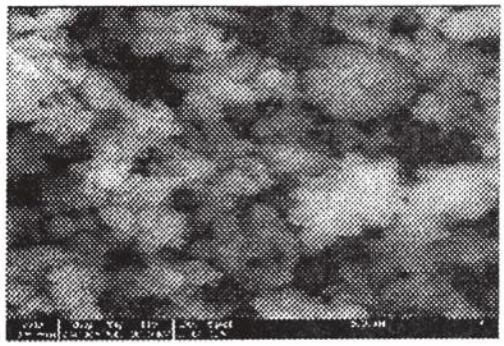

Fig. 2 (i) Morphology of zinc oxide particles prepared without surfactant after 24 hrs growth period.

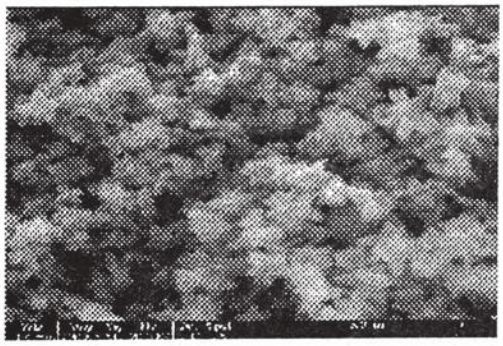

Fig. 2 (ii) Morphology of zinc oxide particles prepared without surfactant after 0.5 hrs growth period.

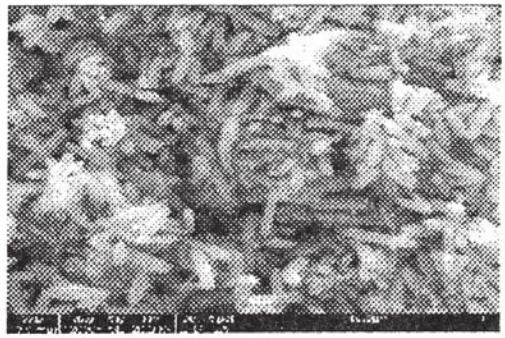

Fig. 2 (iii) Morphology of zinc oxide particles prepared in presence of surfactant (CTAB).

CONCLUSIONS

The particles of zinc oxide are formed when zinc acetate dihydrate and sodium hydroxide are allowed to react in open atmosphere at 70°C. The particles diffuse in the solution after the formation and segregate to grow. The buoyancy helps the growth of the particles to a certain limit till the buoyancy of solvent obeys the laws of floating bodies. When the size of particle exceeds the buoyancy force the particles sink and growth of the particles ceases. To minimize the size of particles, the buoyancy of the solution should be reduced. Therefore, dilute solutions will help the formation of nanoparticles.

REFERENCES

1. K. Nomura, H. Ohta, K. Ueda, T. Kamiya, M. Hirano and H. Hosono, Thin-Film Transistor Fabricated in Single-Crystalline Transparent Oxide Semiconductor, Science, 300, 1269, (2003).

2. H. Harima, "Raman studies on spintronics materials based on wide bandgap semiconductors", J. Phys. Condensed Mater. 16, S5653, (2004).

3. X.L. Cheng, H. Zhao, L.H.Huo, S. Gao, and J.G. Zhao., "ZnO nanoparticulate thin film: Preparation, characterization and gas sensing property", Sens. and Actuators B, 102, 248, (2004).

4. D. C. Look, Mater, "Recent advances in ZnO materials and devices", Sci. Eng. B, 80, 381, (2004).

5. D. C. Look., "Production and annealing of electron irradiation damage in ZnO", Appl. Phys. Lett. 75, 811, (1999).

6. J. Fallert, R. Hauschild, F. Stelzl, A. Urban, M. Wissinger, H. Zhou, C. Klingshirn, and H.Kalt., "Surface state related luminescence in ZnO nanocrystals", J. Appl. Phys., 94, 2895, (2003).

7. Bin Liu, H. C. Zeng, J. Am. Chem. Soc. 125, 4430-4433, (2003).

8. Hui Zhang, Deren Yang, Yujie Ji, Xiangyang Ma, Jin Xu, and Duanlin Que., "Low temperature synthesis of flowerlike ZnO nanostructures by Cetyltrimrthylammonium Bromide-assisted hydrothermal process" J. Phys. Chem. B, 108, 3955-3958, (2004).

9. J. Tang, X. Cui, Y. Liu and X. Yang., "Morphology-controlled synthesis of monodisperse ZnO trough at the air-water interface under mild condition", J. Phys. Chem. B, 109, 22244-22249, (2005).

10. K.Govender, D.S.Boyle, P.B. Kenway and P. O'Brien, "Understanding the factors that govern the deposition and morphology of thin films of ZnO from aqueous solution", J. Mater. Chem. 14, 2575-2591, (2004).

11. N.S. Pesika, Z Hu, K.J. Stebe, and P.C. Searson., "Quenching of growth of ZnO nanoparticles by adsorption of octanethiol", J. Phys. Chem. B, 106, 6985-6990, (2002).

12. N. LÜ, X.LÜ, X. Jin and C. LÜ,et al., "Preparation and characterization of UV-curable ZnO/polymer nanocomposite films", Polym. Int. 56, 138-143, (2007).

13. A.H. Ansari, F. Mohammad and S.P. Ansari., "Production of zinc oxide nanoparticles at atmospheric pressure and low temperature", Patent application No. 235/DEL/2008.

EFFECT OF COMPOSITION AND SINTERING ATMOSPHERE ON PHASE BALANCE OF P/M DUPLEX STAINLESS STEELS

R Mariappan[1], S Kumaran[2], T Srinivasa Rao[2], V Muthupandi[2]

[1] Department of Metallurgical and Materials Engineering
National Institute of Technology, Tiruchirappalli, Tamil Nadu.

ABSTRACT

Duplex stainless steels (DSS) are finding ever increasing applications because of their improved corrosion resistance in combination with strength. These properties could be achieved from controlled phase balance which is a result of tight composition control and heat treatment. Though majority of the DSS are produced through melt route some of the applications call for DSS components produced through powder metallurgy route (PM-DSS). Phase balance of PM-DSS is influenced by the composition and the sintering procedure. In the current investigation PM-DSS of two different compositions were obtained by mixing pre-alloyed stainless steels and elemental powders in different proportions. Compacts were sintered either in vacuum or hydrogen environment. Density of the sintered specimens was estimated from the mass and physical dimensions of the compacts. Ferrite content was measured with different techniques such as point count method, X-ray diffraction and using Fischer ferritscope. Results obtained are presented and the influence of composition and sintering atmosphere on ferrite phase balance is discussed.

1. INTRODUCTION

Duplex stainless steels (DSS) are characterized by an outstanding combination of strength, toughness and corrosion resistance. Ferritic and austenitic stainless steels have low temperature toughness and inferior stress corrosion resistance respectively, whereas duplex stainless steels have properties which are combination of the best properties of these two [1]. Combination of such properties makes duplex stainless steels very attractive for numerous applications. Duplex stainless steels produced through powder metallurgy (P/M) route also find many industrial applications. Typical applications for P/M duplex stainless steels are flanges, valve bodies, fittings, pumps, mixers, and manifold sections [2-5]. Powder metallurgy enables production of duplex stainless steels by several methods. The first method is based on fully pre-alloyed powder with a required duplex composition [6]. The approach for the next one is mixing the elemental powders such as Cr, Ni, Mo powders with austenitic and ferritic stainless steel powders in proper ratios to ensure required ferrite–austenite ratio [7-9]. Sintering is the most important step in P/M process which influences phase balance as well as mechanical properties of the sintered stainless steel components. Recent research efforts are on the prediction of the proportions of two phases in the DSS, because phase balance has a direct impact on corrosion and mechanical properties. Traditionally, the effects of different alloying elements on phase balance have been quantified by using the nickel and chromium equivalent numbers. In addition to the chemical composition other important factors influencing the phase balance in P/M duplex stainless steels are sintering temperature, sintering atmosphere and cooling rate [10]. In the present work two different compacts of DSS were developed from pre-mixture of 316L and 430L powders mixed along with and without Cr, Ni and Mo elemental powder and subsequently sintered in two different atmospheres (hydrogen and vacuum) and the influence of sintering atmospheres on phase balance, and microstructure were investigated and analysed.

EXPERIMENTAL PROCEDURE

Duplex stainless steels of two different compositions viz., A and B were produced using water atomized 316L austenitic and 430L ferritic stainless steel powders mixed with or without elemental powders such as Cr, Mo and Ni to produce P/M DSS. These powders were supplied by M/s Hoganas India Ltd. The chemical compositions of 316L and 430L powders are listed in table1 and compositions A and B are given in table2. Fig.1 shows the morphology of the powder mix of compositions A and B.

Table1: Chemical composition of 316L and 430L powders

Powder Grade	Cr	C	Ni	Si	Mn	Mo	Fe	Flow Rate/ 50 g (sec)	Apparent Density (g/cm³)
316L	16.60	0.02	12.43	0.90	0.10	2.10	Balance	25.4	2.77
430L	16.56	0.01	--	1.20	0.10	----	Balance	27.4	2.88

Table 2: Chemical composition of duplex stainless steels

Powder Mixtures	Composition A (50%316L +50%430L) wt% Composition B (45%316L+45% 430L +4 %Cr+3%Mo+3%Ni) wt%						
Composition Designation	Elements Concentration(%wt)						
	Cr	C	Ni	Si	Mn	Mo	Fe
	A	16.58	0.018	6.22	1.05	0.10	1.10 Bal
	B	18.93	0.016	8.59	0.95	0.09	3.95 Bal

Cylindrical green compacts of 30mm diameter and 12mm height prepared at 560MPa were sintered at 1350°C for 4 hrs in two different controlled atmospheres viz., partial vacuum and hydrogen in an electrically heated muffle furnace. During vacuum sintering the pressure level was maintained at 10-1 mbar with hydrogen as the back filling gas. As the vapor pressure of

chromium at 1350°C is 1.073 x 10-2 mbar, no loss of Cr due to evaporation at 10-1 mbar was expected at the sintering temperature. Sintering in hydrogen environment was carried out by maintaining a positive pressure in the furnace chamber by passing 250 ml of hydrogen per

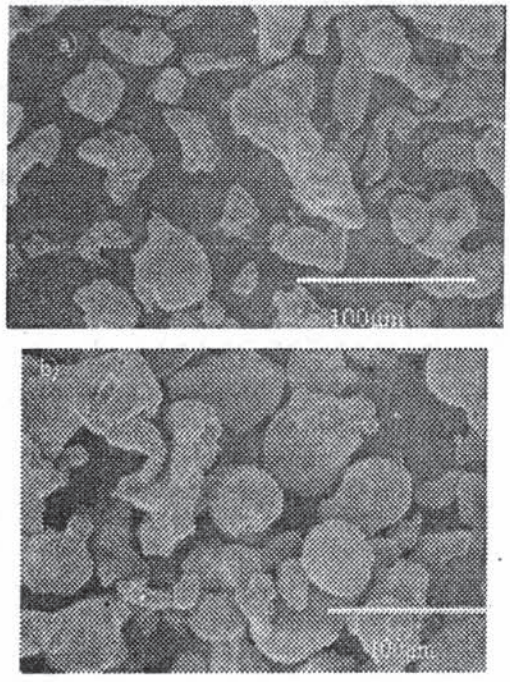

Fig.1 SEM micrograph of DSS Powder a) composition A, b) composition B

minute. After sintering, compacts were cooled to 200°C at the rate of 45 to 50°C per minute and after that they were allowed to cool to room temperature along with the furnace. In order to understand the effect of sintering on densification behavior density of both green and sintered compacts was measured by mass and physical dimensions. Microstructural analysis was made with the help of image analyzer. Phases present in the sintered steels were identified from X-ray diffraction pattern obtained with Cu Kα radiation using a Rigaku diffractometer. The ferrite content of the sintered products was estimated with Fischer feritscope and also by metallographic point count method. Densification parameter was calculated by using the following formula:

$$\Delta D = (\text{sintered density} - \text{green density}) / (\text{theoretical density} - \text{green density})$$

RESULTS AND DISCUSSION

Densification Properties

Table 3 shows the densities of DSS compacts sintered in hydrogen and vacuum atmospheres. Densification behaviour of duplex stainless steels compacts is better in vacuum sintering than in hydrogen atmosphere. Attention is drawn in the procedure adopted in maintaining the vacuum environment; use of a soft vacuum of 10-1 mbar with hydrogen backfilling offered the advantages of both vacuum and hydrogen environment.

Table.3 Densities of duplex stainless steels sintered in hydrogen atmosphere

Composition	Compaction Pressure 560 MPa					
	Hydrogen atmosphere				vacuum atmosphere	
	Green Density (g/ cm³)	Theoretical Density (g/cm³)	Sintered Density (g/cm³)	Densification Parameter (ΔD)	Sintered Density (g/cm³)	Densification Parameter (ΔD)
A	6.343	7.95	7.395	0.6547	7.668	0.7945
B	6.235	8.01	7.270	0.6380	7.661	0.8033

Microstructural Evaluation

Microstructures of DSS of compositions A and B sintered in hydrogen and vacuum atmospheres are shown in Figures 2 and 3, respectively. Wrought duplex stainless steels are generally designed to primarily solidify as ferrite and part of this will transform in to austenite when cooled below the solvus temperature from where these steels are quenched in water to room temperature in order to retain high temperature two-phase structure and to avoid formation of undesirable intermetallics or secondary phases. In the case of DSS produced through powder metallurgy route equilibrium phases at sintering temperature are established provided sufficient time is given for equilibration of composition by diffusion. In the present study all the sintered compacts were cooled in the furnace itself at the rate of 45 to 50°C per minute. Therefore the final microstructure of these sintered compacts is decided by the C- curves of the phases and intermetallics involved in DSS. C-curves in turn are function of composition and therefore the final microstructure in the sintered compacts are the results of their respective composition. Since DSS are fine grained steels the morphology of ferrite and austenite can have little effect while their relative amount can influence the properties to a greater extent. Composition A has less of ferrite formers than in Composition B. Therefore it is no surprise to observe more amount of austenite in A than in B. Moreover Composition B is enriched with chromium and molybdenum. These elements promote formation of more ferrite and small amount black regions. Though attempts were not made to characterize these black regions seen in Fig 2b, based on the previous knowledge on heat treated wrought duplex stainless steels it is presumed that they could be sigma phase.

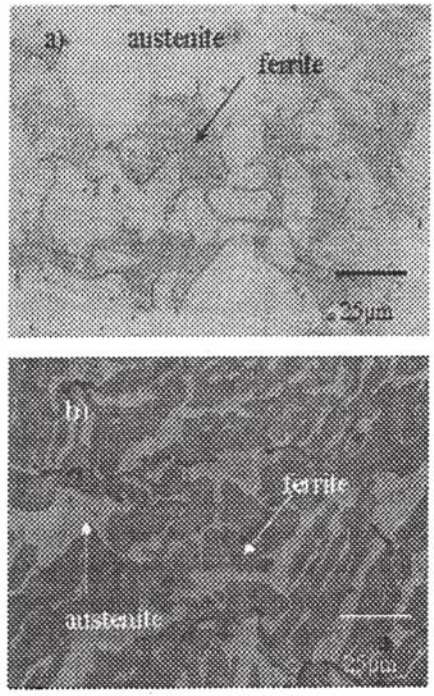

Fig.2 Microstructures of DSS (a) composition A and (b) composition B, sintered in hydrogen atmosphere

Figure 3 shows the microstructure of compositions sintered under partial vacuum. Though the compositions are different only marginal variation in phase balance could be noticed in the microstructures of compacts of compositions A and B sintered in partial vacuum. Influence of Cr, Mo on ferrite formation is compensated by the addition of austenite forming Ni in

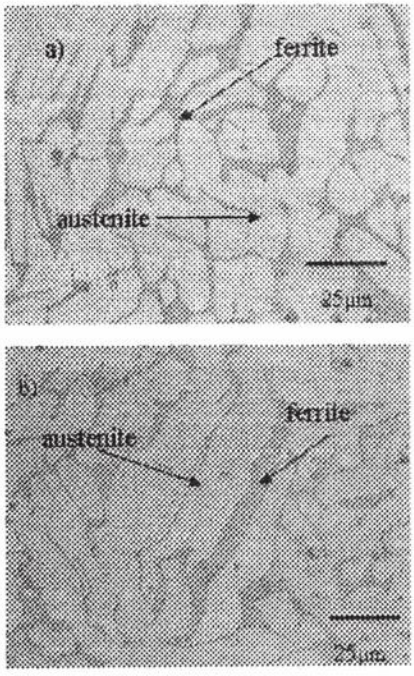

Fig.3 Microstructures of DSS (a) composition A and (b) composition B, sintered in partial vacuum

composition B. Further the microstructures show that whether the duplex stainless steel was prepared from pre alloyed powders or by using elemental powders the resulting phase balance is decided only by the overall composition if sintering is carried out in partial vacuum. The reducing environment prevailing due to the backfilling with hydrogen combined with partial vacuum prevented oxidation, if not reducing the existing oxides and helped in attainment of equilibrium composition. For identical compositions and cooling rates from sintering temperature sigma phase formation is avoided in the case of vacuum sintering while presence of sigma phase could be noticed (Fig 2b and 3b) in compacts sintered in hydrogen atmosphere. Possibly vacuum sintering would have experienced a slightly higher cooling rate than sintering in hydrogen atmosphere.

Ferrite Content Measurement

Ferrite volume percentage in P/M sintered duplex stainless steels estimated by using Fischer's feritscope and metallographic point count method are given in table 4. Metallographic point count method is an absolute quantitative metallographic technique while the measurements made with feritscope is influenced by the phase composition. Therefore some amount of variations is expected between the values obtained by these two techniques. However, instrumental techniques in estimation of ferrite content are extensively used in industries due to its simplicity in operation and rapidity in getting the results.

Composition A shows higher ferrite content than composition B when sintered in vacuum and the results are reversed for sintering in hydrogen atmosphere. Though sintering temperatures were same there could be slight variation in the cooling rates. In duplex stainless steels equilibrium phase content at the sintering temperature is decided by the composition and corresponding nickel and chromium equivalents. For the same steels phase balance at room temperature is decided not only by the equilibrium and also by the cooling rate experienced by the sintered compacts. Further the slope of the solvus line in the quasibinary phase diagram of duplex stainless steels depends on the composition. When the solvus line is sloping for low nickel equivalents it remains more or less vertical for higher nickel equivalents. For DSS having vertical solvus line cooling rate from the sintering temperature has least influence on the room temperature phase balance and therefore austenite ratio is more or less same for both at sintering and room temperatures. Hence DSS of composition B does not show much variation in its ferrite content while the ferrite content for composition A varies with sintering environment for composition A.

Table.4 Ferrite content of duplex stainless steels sintered in different atmospheres

Composition	Vacuum Atmosphere		Hydrogen Atmosphere	
	Fischer Ferrite scope (% Ferrite)	Point Count Method (% Ferrite)	Fischer Ferrite scope (% Ferrite)	Point Count Method (% Ferrite)
A	44-47	45 - 49	28-30	31 - 33
B	32-35	32 - 39	37 -39	38 - 42

XRD PATTERNS

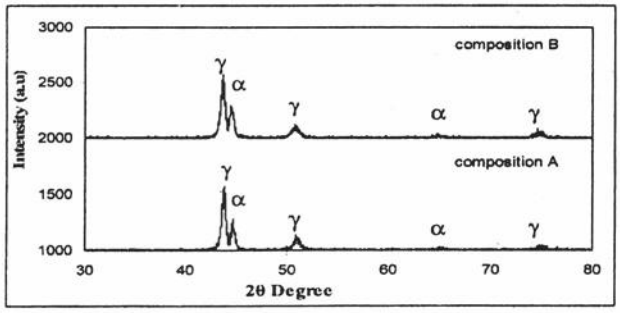

Fig.4 XRD patterns of duplex stainless steels sintered in hydrogen atmosphere

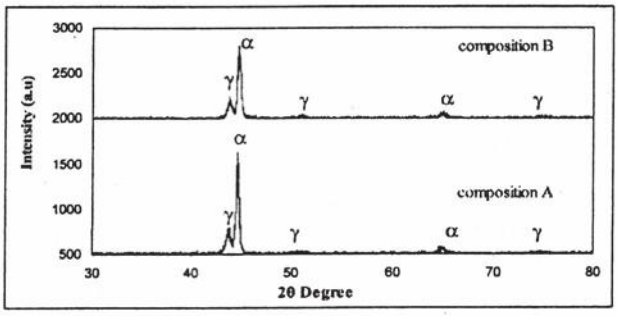

Fig.5 XRD patterns of duplex stainless steels sintered in partial vacuum

XRD patterns of duplex stainless steels sintered in hydrogen and partial vacuum are shown in Figures 4 and 5, respectively. For both the compositions sintering in hydrogen atmosphere resulted in higher austenite content than sintering in vacuum. This characteristic feature is revealed by the relative heights of the prominent ferrite and austenite peaks. The results suggest that sintering in hydrogen environment is preferable than sintering in vacuum.

CONCLUSION

The aim of the present work was to study the effect of chemical compositions and sintering atmosphere on phase balance of P/M duplex stainless steels. The salient features of the present study are as follows:

- Duplex stainless steels sintered under partial vacuum exhibit better sintered density and densification parameter than stainless steels sintered in hydrogen atmosphere.
- Duplex stainless steels with high Cr and Ni equivalents exhibit more or less same phase balance irrespective of the sintering atmosphere.

ACKNOWLEDGEMENTS

The authors would like to thank Dr. M. Chidambaram, Director, NIT, Tiruchirappalli-620 015 for providing financial support and permission to present this research paper. Authors would also like to acknowledge the Centre for Nano Materials, ARCI, and Hyderabad for providing the facilities to carry out the sintering process.

REFERENCES

[1]. P. Datta, G.S. Upadhyaya, Sintered duplex stainless steels from premixes of 316L and 434L powders, Materials Chemistry and Physics, Vol. 67 (2001), pp.234-242.

[2]. L.A. Dobrza ski, Z. Brytan, M. Actis Grande, M. Rosso, E. J. Pallavicini, Properties of vacuum sintered duplex stainless steels, Journal of Materials Processing Technology, Vol. 157-158 (2004), pp. 312-316.

[3]. P.K. Samal, J. B. Terrell, Mechanical properties improvement of PM 400 series stainless steels via nickel addition, Metal Powder Report, December 2001, (2001) pp. 28-34.

[4]. A. J. Rawlings, H. M. Kopech, H. G. Rutz, The effect of service temperature on the properties of ferritic P/M stainless steels, Proceedings of International Conference on Powder Metallurgy & Particulate Materials PM2TEC'97, Chicago USA (1997).

[5] Engstrom U., Copper in P/M Steels, Int. J. Powder Metall., 2003; 39(4): 29-39.

[6] C.J. Munez, M.V. Utrilla, A. Urena, Effect of temperature on sintered austeno-ferritic stainless steel microstructure, Journal of Alloys and Compounds (2007).

[7] J. Kaziora, M. Nykiela, T. Pieczonkab, T. Marcu Puscasc, A. Molinaric, Activated sintering of P/M duplex stainless steel powders, Journal of Materials Processing Technology ,157–158, (2004), pp712–717.

[8] Olena Smuk, Microstructure and properties of modern P/M super duplex stainless Steel, doctoral thesis, Dept. of Mat. Sci.and Eng., Royal Institute of Technology, Sweden (2004) pp1-5.

[9] F. Iacoviello, M. Boniardi, G.M. La Vecchia Analysis of stress ratio effects on fatigue propagation in a sintered duplex steel by experimentation and artificial neuralnetwork approaches, International Journal of Fatigue, 21,(1999),pp957-963.

INFLUENCE OF CARBON CONTENT ON WORKABILITY BEHAVIOR OF POWDER METALLURGY STEELS

R.Narayanasamy [1,], V.Anandakrishnan [1], S.Sivasankaran [1], K.Siva Prasad [2], K.S.Pandey [3]*

[1] Department of Production engineering,
[2] Department of Metallurgical and Materials Engineering, National Institute of Technology, Thiruchirappalli.
[3] Maulana Azad National Institute of Technology, Bhopal.

ABSTRACT

A complete experimental investigation on the workability behavior of sintered ferrous powder metallurgy preforms of pure iron, 0.4% and 0.8% carbon steels having two different aspect ratios, namely, 0.39 and 0.59 with graphite lubricant was carried out during cold upsetting. Also a novel formability stress index is proposed based on the yield criteria developed by Narayanasamy et al, compared with the one developed by Doraivelu et al and presented. Using the abovementioned mathematical yield theories the various stress ratio parameters, namely, hoop stress to effective stress and axial stress to effective stress were evaluated under triaxial stress state condition and their relationship with axial strain is plotted, analyzed and discussed. The investigation reveals that as the carbon content increases the formability stress index for higher aspect ratio was found to be higher because of the reduction in pore size which is evidential by as-sintered preform's scanning electron microscopic images.

1. INTRODUCTION

Powder metallurgy (P/M) processing is a net or near net-shaped production technology which eradicates the need for most of the secondary machining operations. Automotive and off-highway vehicle applications dominate the ferrous P/M structural parts market. However, there are many other fields where ferrous P/M parts are used such as lawn, garden structural parts, hand tools, hobby applications, household appliances, lock hardware, industrial motors, controls, hydraulic applications, etc., and satisfies close dimensional tolerance requirements for parts even with complex geometries [1]. Workability is the ability of a material to endure the induced internal stresses of forming former to the occurrence of splitting of material. It is a convoluted technological perception that depends not only on the material but also the various process parameters such as strain, strain rate, stress, friction, temperature, etc. Workability of porous steel performs was discussed by Aly El-Domiaty and Mostafa Shaker [2]. Later Abdel-Rahman et al [3] proposed a workability factor (β) for describing the effect of the mean stress and the effective stress with the help of two theories and the effect of relative density was discussed. Soon after, computer aided systems for determination and evaluation of workability were developed by Wifi et al [4] and Petruska and Janicek [5]. A mathematical theory of plasticity for compressible powder metallurgy materials was developed by Narayanasamy et al [6]. In the present work the workability behaviour of sintered powder metallurgy pure iron, 0.4% and 0.8% carbon steels were experimentally investigated completely. The afore-said P/M preforms with different aspect ratios, namely, 0.39 and 0.59 were subjected to cold deformation with graphite lubricant and their formability behaviour under triaxial stress state condition was studied, discussed and reported. The workability index was determined using two different yield criterions developed by Doraivelu et al., and Narayanasamy et al. and a comparison was made between them. The variations of formability stress parameter with respect to axial strain were plotted for the above-said three different powder metallurgy preforms having two different afore-said aspect ratios. Also the characteristics of various stress ratio parameters such as axial stress to effective stress ($\sigma z/\sigma eff$), and hoop stress to effective stress ($\sigma\theta/\sigma eff$) with respect to axial strain (εz) were evaluated and presented.

2. EXPERIMENTAL DETAILS

Atomized iron powder of −150 μm with 99.7% purity was used. The characteristics of iron powder were studied by determining the flow rate, the apparent density and the particle size distribution and the observations are

given in Table 1. Fig. 1(a) shows the SEM photograph of iron powder. Powder mix corresponding to pure iron, Fe–0.4%C and Fe–0.8%C were blended on a pot mill to obtain a homogeneous powder blend. The mesh size of carbon powder mixed had fallen between 5 μm and 10 μm. Green compacts of the powder blend with initial preform density of 84% of the theoretical density were prepared on a 1.0MN capacity hydraulic press using suitable punch and die setup. The free surfaces of the compacts were coated with an indigenously developed ceramic mixture [7]. The ceramic-coated compacts were sintered in an electric muffle furnace in the temperature range of (1120±10)°C for a sintering time of 120 min and allowed to get cooled to room temperature in the furnace itself. The microstructure of as-sintered pure iron showing spheroidization of pores in black color, the ferrite white regions and few regions of eutectoid (pearlite) is shown in Fig. 1(b). Addition of 0.4% carbon which resulted in reduced pores and more amount of eutectoid (pearlite) with white background of ferrite grains are shown in Fig. 1(c). As-sintered 0.8% carbon steel contains very few pores with ferrite/pearlite microstructure as shown in Fig. 1(d). All the above-said microstructures showed elimination of grain boundaries and spheroidization of pores due to higher sintering temperature and time.

TABLE 1 Characterization of iron powder

Characteristics	Iron
Apparent density (g/cm³)	3.26
Flow rate (s) per 50 g	24.5
Compressibility (g/cm³) at a pressure of (400±10) MPa	6.20
Sieve analysis: Sieve size (μm)	+150, +125, +106, +90, +75, +63, +53, +45, +37, –37
Percent distribution (weight)	3.88, 20.21, 9.10, 3.40, 20.80, 17.92, 4.60, 1.91, 3.72, 3.20

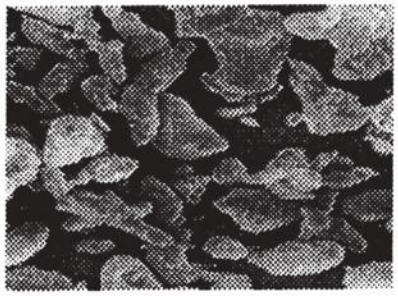

Fig. 1. (a) The SEM photograph of Iron powder and

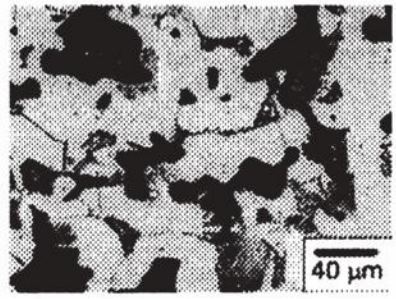

(b) Microstructure of as-sintered P/M pure iron

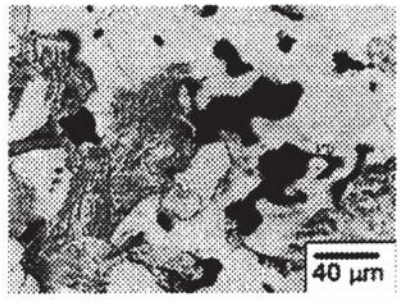

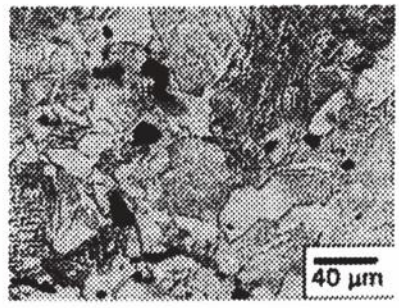

Fig. 1. Microstructure of as-sintered P/M (c) 0.4% carbon steel and (d) 0.8% carbon steel.

The ceramic coatings over the specimen were machined off and further machining was carried out to such dimensions, so that to obtain preforms with initial aspect ratios 0.39 and 0.59. Initial diameter (D0), initial height (h0) and the initial preform relative density (ρ0) of the specimen were measured and recorded. Each compact was subjected to the incremental compressive loads of 0.05MN and the upsetting was carried between two flat, mirror finished open dies on a hydraulic press of 1.0MN capacity. The deformation was carried out until the appearance of the first visible crack on the free surface. In order to get a quite homogeneous deformation, graphite lubricant was applied on both of the die contact surfaces during cold deformation, which also ensured the absolute minimum friction condition. After each interval of loading dimensional changes in the specimen such as height after deformation (hf), top contact diameter (DTC), bottom contact diameter (DBC), bulged diameter (DB) and density of the preform (ρf) were measured. The density of forged preforms was determined after every

loading interval using the Archimedes principle [8]. The schematic showing the various parameters measured before and after deformation is given in Fig. 2.

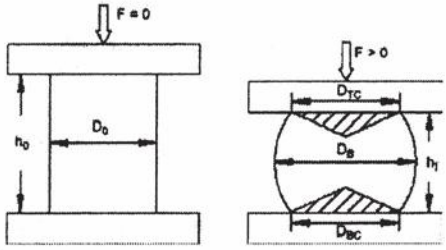

Fig. 2. Upset forging test preforms before and after deformation

3. THEORITICAL DISCUSSION

The measurements made before and after each compressive incremental loading were used to calculate the true axial stresses and strains, which provided the basis for the determination of various parameters. The mathematical expressions used and proposed for the determination of various upsetting parameters under triaxial stress state condition were discussed below:

3.1 Strains

During the compression of a P/M part under frictional conditions, the average density increases. Friction enhances densification and at the same time decreases the height reduction at fracture.

The true axial or height strain ( ) is given as:

$$\varepsilon_z = \ln\left(\frac{h_f}{h_0}\right) \tag{1}$$

The hoop strain ( ) is given by the following equation as explained by Narayanasamy et al. [9]

$$\varepsilon_\theta = \ln\left(\frac{2D_B^2 + D_C^2}{3D_0^2}\right) \tag{2}$$

Where,

DB is the bulged diameter of the preform after deformation

DC is the contact diameter of the preform after deformation

D0 is the initial diameter of the preform before deformation

h0 is the initial height of the preform before deformation and

hf is the height of the preform after deformation.

When the upsetting continues, the final diameter increases and the corresponding hoop strain( ), which is tensile in nature, also increases until it reaches the fracture limit.

3.2 Triaxial Stress State Condition

According to Narayanasamy et al. [9] the state of stress in a triaxial stress condition is given as follows:

$$\alpha = \left(\frac{A}{B}\right) \tag{3}$$

where,

$A = [(2+R^2)\sigma_\theta - R^2(\sigma_z + 2\sigma_\theta)]$; $B = [(2+R^2)\sigma_z - R^2(\sigma_z + 2\sigma_\theta)]$;

α is Poisson's Ratio; R is Relative Density;

σ_z is the axial stress and σ_θ is the hoop stress.

The determination of axial stress σz is carried out from the measured values of contact areas and the corresponding load applied.

In triaxial stress condition for the known values of Poisson's ratio(α),relative density(R) and axial stress (σz), the Hoop stress component (σθ) can be determined as explained by Narayanasamy et al. [10] as follows:

$$\sigma_\theta = \left(\frac{2\alpha + R^2}{2 - R^2 + 2R^2\alpha}\right)\sigma_z \tag{4}$$

In the above equation (4), the relative density (R) plays a major role in finding the hoop stress component ( ).

The hydrostatic stress is given by,

$$\sigma_m = \frac{(\sigma_1 + \sigma_2 + \sigma_3)}{3} \tag{5}$$

In terms of cylindrical coordinates the equation (5) becomes as follows:

$$\sigma_m = \frac{(\sigma_z + \sigma_r + \sigma_\theta)}{3} \tag{5a}$$

Since for axisymmetric or cylindrical upsetting, the above equation (5a) becomes as follows:

$$\sigma_m = \frac{(\sigma_z + 2\sigma_\theta)}{3} \tag{6}$$

3.2.1 Yield equations

The effective stress can be determined by the Doraivelu et al [11] equation, Narayanasamy et al [12] equation as follows:

According to Doraivelu et al [11] the effective stress for porous material is

$$[\sigma_1^2 + \sigma_2^2 + \sigma_3^2 - R^2(\sigma_1\sigma_2 + \sigma_2\sigma_3 + \sigma_3\sigma_1)] = (2R^2 - 1)\sigma_{eff}^2 \tag{7}$$

The above equation can be written in terms of cylindrical coordinates as follows:

$$\sigma_{eff}^2 = \frac{\left[\sigma_z^2 + \sigma_\theta^2 + \sigma_r^2 - R^2(\sigma_z\sigma_\theta + \sigma_\theta\sigma_r + \sigma_r\sigma_z)\right]}{2R^2 - 1} \quad (8)$$

Since σθ = σr, for axisymmetric or cylindrical upsetting, the equation (8) can become as follows:

$$\sigma_{eff} = \left(\frac{\left[\sigma_z^2 + 2\sigma_\theta^2 - R^2(\sigma_\theta^2 + 2\sigma_z\sigma_\theta)\right]}{2R^2 - 1}\right)^{1/2} \quad (9)$$

In the above equation (9), for the known values of σz, σθ and R, the effective stress σeff can be determined.

According to Narayanasamy et al [12] the general yield equation for porous material is

$$(2+R^m)\left[\frac{(\sigma_1-\sigma_2)^m + (\sigma_2-\sigma_3)^m + r^m(\sigma_3-\sigma_1)^m}{(2+r^m)(1+r^m)}\right] + \left[\frac{3}{(2+r^m)}\right]^m \frac{(1-R^m)(\sigma_1+\sigma_2+\sigma_3)^2}{3} = \frac{\sigma_{eff}^2(R-R_c)^2}{(1-R_c)^2} \quad (10)$$

Where,

m = yield criterion constant (m = 2); r = anisotropy parameter;
r^p = anisotropy parameter, p is a constant (r^p = 1); R = relative density of P/M preform;
R_c = critical relative density, for iron R_c = 0.654; σ_{eff} = effective stress;
$\sigma_1, \sigma_2, \sigma_3$ = principal stresses at three different directions.

after substituting the values of m = 2, rp = 1, Rc = 0.654, n = 2, in equation (10) and the equation in terms of cylindrical coordinates such as σ1 = σz, σ2 = σθ, σ3 = σr as follows:

$$\sigma_{eff} = \left[\frac{(1-0.654)^2}{(R-0.654)^2}\left[(\sigma_z^2 + 2\sigma_\theta^2) - R^2(\sigma_\theta^2 + 2\sigma_\theta\sigma_z)\right]\right]^{1/2} \quad (11)$$

In the above equation (11), for the known values of σz, σθ and R, the effective stress σeff can be determined.

3.3 Fromability stress index (βσ)

As an evidence of experimental investigation implying the importance of the spherical component of the stress state on fracture, Vujovic and Shabaik [13] proposed a parameter called a Formability Stress Index 'βσ' is given by,

$$\beta_\sigma = \left(\frac{3\sigma_m}{\sigma_{eff}}\right) \quad (12)$$

This index determines the fracture limit as explained in the reference [9].

4. RESULTS AND DISCUSSION

Figs. 3(a) and (b) have been plotted between the formability stress parameter (βσ) and the axial strain (εz) for steel containing different carbon percentage and for two different aspect ratios namely 0.39 and 0.59. In general, as the carbon content increases the slope value between the formability stress parameter (βσ) and the axial strain (εz) also increases. In the present case the size of graphite powder is very small (which is in the order of 5–10 μm) and occupies the pores created between iron particles. Because of this reason, the pore size is very small and takes higher formability stress value during plastic deformation. In the case of pure iron the pore size is bigger compared to 0.4% and 0.8% carbon steel and this result in lower formability stress value. It is further notified that as the pore size becomes smaller and smaller as in the case of 0.8% or 0.4% carbon steel, the formability stress value increases to higher value. As the aspect ratio increases in the case of pure iron the slope value increases to higher value as shown in Fig. 3(b). This indicates that the aspect ratio value 0.59 is also smaller value and this shows better densification as far as pure iron is concerned. As pointed out in Fig. 3(a) and (b), the slope value between the formability stress parameter (βσ) and the axial strain (εz) continues to be higher for the case of 0.4% carbon steel among the steels tested. The increase in carbon content beyond 0.4% does not help as far as densification rate is concerned. However, as the carbon content increases the pores size decreases and shows better formability stress value. Though, it was found from the Figs.3.(a) and (b) that both the equations predicted the same behavior, but the formability stress index determined based on Narayanasamy et al's criterion [12] is higher than that of Doraivelu et al's criterion [11]. The reason for the above difference is due to the consideration of yield criteria constant, anisotropy parameter and critical relative density for the determination of effective stress in Narayanasamy et al's criterion [12].

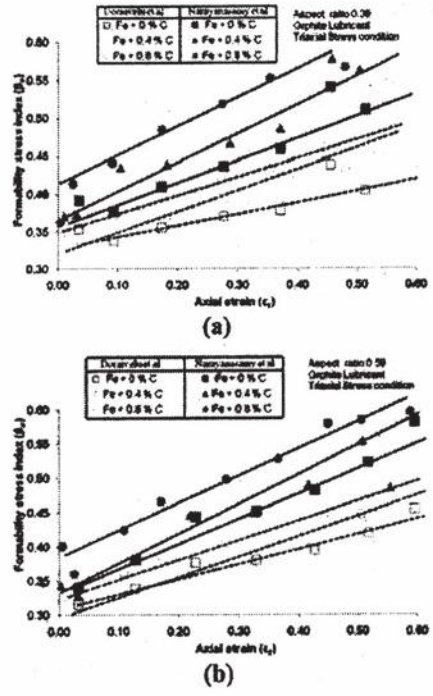

Fig.3. The variation of F ormability Stress Index (βσ) with respect to the axial strain (εz) for aspect ratio (a) 0.39 and (b) 0.59.

Fig. 4(a) and (b) has been plotted between the stress ratio parameter (σz/σeff) and the axial strain (εz) for steel containing three different carbon percentage and for two different aspect ratios namely 0.39 and 0.59. In general, as the carbon content increases the slope value between the stress ratio parameters (σz/σeff) and the axial strain (εz) also increases rapidly during deformation. As the carbon content increases the stress ratio parameter (σz/σeff) is found to be higher compared to pure iron with no carbon content. In the case of pure iron, the pore size is larger compared to carbon steels and this result in lower stress ratio parameter (σz/σeff) value for pure iron. As the aspect ratio increases the densification rate value and the stress ratio parameter (σz/σeff) also increases with increase in carbon content. Figs.4.(a) and (b) that both the equations predicted the same behavior, but the stress ratio parameter (σz/σeff) determined based on Narayanasamy et al's criterion [12] is higher than that of Doraivelu et al's criterion [11]. The reason for the above difference is due to the consideration of yield criteria constant, anisotropy parameter and critical relative density for the determination of effective stress in Narayanasamy et al's criterion [12].

It was found from the Fig.4. (a) and (b) that both equation predicted the same behavior.

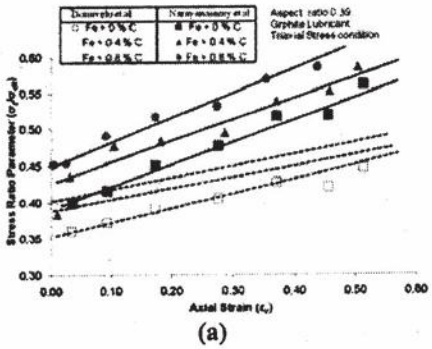

(a)

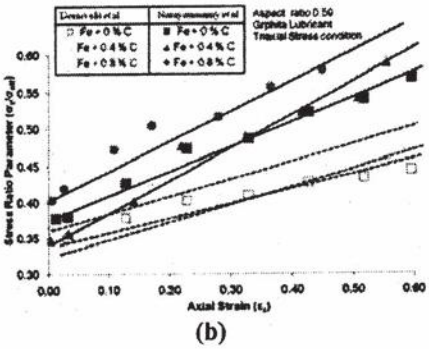

(b)

Fig. 4. The variation of stress ratio parameter (σz/σeff) with respect to the axial strain (εz) for aspect ratio (a) 0.39 and (b) 0.59.

Fig. 5(a) and (b) has been plotted between the stress ratio parameter (σθ/σeff) and the axial strain (εz) for steel containing three different carbon percentage and for two different aspect ratios, namely, 0.39 and 0.59 using both the Doraivelu et al and Narayanasamy et al equations. As the deformation increases the hoop stress (σθ) value also increases and therefore this stress ratio parameter (σθ/σeff) also increases with increasing deformation. As the carbon content increases, the pore size is small and takes higher stress ratio parameter compared to steel with no carbon content. In the case of pure iron the pore size is larger and takes lesser value of hoop stress (σθ) during deformation compared to iron with carbon content. Iron with carbon content takes higher stress ratio parameter value because the pore size is very fine. As the aspect ratio increases the stress ratio parameter (σθ/σeff) also increases as indicated by Fig. 5(a) and (b). The reason is the higher aspect ratio 0.59 is ideally suitable for deformation and shows better densification rate compared to lower aspect ratio 0.39. Figs.5.(a) and (b) that both the equations predicted the same behavior, but the stress ratio parameter (σz/σeff) determined based on Narayanasamy et al's criterion [12] is higher than that of Doraivelu et al's criterion [11]. The reason for the above difference is due to the consideration of yield criteria constant, anisotropy parameter and critical relative density for the determination of effective stress in Narayanasamy et al's criterion [12].

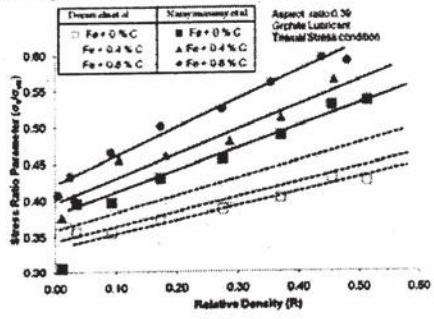

(a)

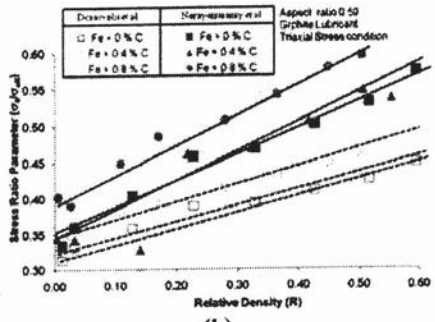

(b)

Fig. 5. The variation of stress ratio parameter (σθ/σeff) with respect to the axial strain (εz) for aspect ratio (a) 0.39 and (b) 0.59

5. CONCLUSIONS

The following conclusions can be drawn from the above results and discussion.

- As the carbon content increases the pore size becomes smaller.
- As the pore size becomes smaller, the formability stress value increases.
- Aspect ratio 0.59 shows higher formability stress value compared to aspect ratio 0.39 because of better densification.
- The stress ratio parameters ($\sigma z/\sigma eff$) and ($\sigma\theta/\sigma eff$) is found to be higher for carbon steels compared to pure iron because of better densification in carbon steels.
- It was found that both the Doraivelu et al and Narayanasamy et al equations exhibited the same behavior and hence both equations are suitable for porous materials to predict the workability phenomenon.
- The formability stress index and the various stress ratio parameters determined based on Narayanasamy et al's criterion [12] is higher than that of Doraivelu et al's criterion [11] due to the consideration of yield criteria constant, anisotropy parameter and critical relative density for the determination of effective stress in the former.

REFERENCES

1. W.B. James, G.T.West, "Ferrous powder metallurgy materials, in: Powder Metal Technologies and Applications", ASM Handbook, Vol. 07, ASM International, pp. 751–768 (2002)
2. Aly El-Domiaty, Mostafa Shaker, J. Mater. Process. Technol. 25 (1991) 229–233.
3. M. Abdel-Rahman, M.N. El-Sheikh, "workability in forging of powder metallurgy compacts", J. Mater. Process. Technol, Vol. 54 (1-4), 97–102, (1995)
4. A.S. Wifi, A. Abdel-Hamid, N. El-Abbasi, "Computer aided evaluation of workability in bulk forming process". J. Mater. Process. Technol, Vol. 77 (1–3), pp.285–293 (1998)
5. J. Petruska, L. Janicek, "Computationally experimental workability determination of compressed cylindrical specimen with surface defects", J. Mater. Process. Technol, 80–81 pp.572–578 (1998)
6. R. Narayanasamy, R. Ponalagusamy, K.R. Subramanian, "Generalized yield criteria of porous sintered powder metallurgy metals", J. Mater. Process. Technol, Vol.110 (2) pp.182–185 (2001)
7. K.S. Pandey, P.S. Misra, M.L. Mehta, "Densification behavior of iron powder preforms during hot upsetting", Trans. PMAI, Vol.13, pp.94–99 (1986)
8. K.H. Moyer, "Measuring density of P/M materials with improved precision", Int. J. Powder. Met. Powder. Technol, Vol.15, pp. 33–42 (1979)
9. R. Narayanasamy, T. Ramesh, K.S. Pandey, "Some aspects on workability of aluminium–iron powder metallurgy composite during cold upsetting", Mater. Sci. Eng. A, Vol.391(1-2), pp.418 – 26 (2005)
10. R. Narayanasamy, T. Ramesh, K.S. Pandey, "Workability studies on cold upsetting of Al–Al2O3 composite material", Mater. Des, Vol. 27(7), pp.566 – 575 (2006)
11. S.M. Doraivelu, H.L. Gegel, J.S. Gunasekara, J.C. Malas, J.T. Morgan, "A new yield function for compressible P/M materials", Int.J.Mech.Sci, Vol.26 (9-12), pp. 527-535 (1984)
12. R. Narayanasamy, R. Ponalagusamy, K.R. Subramanian, "Generalised yield criteria of porous sintered powder metallurgy metals", J. Mater. Process. Technol, Vol. 110, pp. 182-185 (2001)
13. V. Vujovic, A.H. Shabaik, "A New workability criterion for ductile metals", J Eng Mater Technol, Vol.108(3), pp.245–9 (1986)

STUDIES ON MICROSTRUCTURE AND MECHANICAL PROPERTIES OF VACUUM SINTERED STAINLESS STEELS

R. Mariappan[1], S. Kumaran[1], T. Srinivasa Rao[1], S.B. Chandrasekar[2]

Department of Metallurgical and Materials Engineering,
National Institute of Technology, Tiruchirappalli. Tamil Nadu. [1]
Centre for Nano Materials, ARCI, Hyderabad.[2]

ABSTRACT

Three different grades of stainless steels such as ferritic (430L), austenitic (316L) and duplex (combination of 316L and 430L) stainless steels were produced through powder metallurgy route. Initially, the powder samples were compacted at 560 MPa and then sintered at 1350°C for 4hrs in partial vacuum (5x10-2 torr). The sintered stainless steels were characterized with the help of optical microscope, microhardness tester, Hounsfield tensometer and XRD to understand the sintering behaviour of the stainless steels. The vacuum sintered stainless steels exhibited density ranging from 94–96% theoretical density, approximately 14–17% increment from green density. Microstructural analysis showed bi-phase (austenite and ferrite) structure in the duplex composition and other two revealed their respective structures. XRD pattern for duplex composition confirmed this bi-phase structure. The duplex stainless steel exhibited highest tensile strength of 760MPa, with 12% elongation. SEM fractograph of duplex stainless steel revealed dimples of various sizes indicating ductile mode of failure.

1. INTRODUCTION

Technical and economic advantages of the Powder Metallurgy (PM) process have contributed to an increased use of sintered parts for structural applications. Stainless steel powder metallurgy parts play an important role and represent growing segments in the PM industry [1]. These materials in the sintered state have good corrosion resistance and mechanical properties. Particularly, the austenitic type of stainless steels combines these properties. Due to its excellent corrosion and oxidation resistance, good strength and high toughness properties, sintered 316L stainless steel is used to fabricate numerous structural components for applications in the architectural, industrial and nuclear power plant fields [2-4]. Typical applications of P/M 316L stainless steels are in nuclear power plants include filtration, liquid and gas metering, piping flanges and clamps, fasteners, wall/shielding, blanket modules, and ball valves[5-6]. Similarly P/M ferritic grades have found applications in mounting brackets for the rear view mirrors, the tone wheels for the antilock brake systems and also in automotive exhaust applications like exhaust flanges and mounting unit of HEGOS. Sintered stainless steel exhaust flanges and oxygen sensor bosses are produced in bulk for automotive exhaust systems. Duplex stainless steels obtained by powder metallurgy technology could be used in many industrial branches due to their high mechanical properties and good corrosion resistance [7-9]. P/M+HIP (hot isostatic pressing) duplex stainless steels have already shown their potential applications in process industry, off shore, pulp and paper industry [10]. Typical applications for P/M duplex stainless steels are flanges, valve bodies, fittings, pumps, mixers, and manifold sections. The ongoing efforts are aimed at improving the properties of P/M stainless steel through compositional and sintering modifications. Fully dense P/M stainless steels are made predominantly from spherically shaped, inert gas atomized stainless steel powders by extrusion, hot isostatic pressing, and metal injection molding (MIM). The mechanical properties, as well as corrosion resistance of parts produced by these techniques, are generally similar to those of their conventional wrought counterparts. High density stainless steels can be produced by P/M forging, but high temperature sintering is the preferred fabrication method. Sintering at higher temperature and longer duration enhances the corrosion resistance and mechanical properties[11-12]. In the present investigation three different stainless steels, namely 316L, 430L and DSS were prepared from premixes of 316L, 430L powders and subsequently sintered at 1350°C for 4 hrs in partial vacuum (5x10-2 torr). The microstructure and mechanical properties of these steels were analyzed.

2. EXPERIMENTAL DETAILS

Water atomized 316L austenitic and 430L ferritic stainless steel powders supplied by M/s Hoganas India Ltd. were used in the present work. Austenitic, ferritic and duplex stainless steel preforms were produced through P/M route using vacuum sintering to study microstructure and mechanical properties. The SEM micrographs of the 316L and 430L pre-alloyed powder particles are shown in fig.1a and fig.1b respectively. Ferritic grade powder particles are coarser than austenitic grade power and both are having irregular shape. The chemical compositions and sieve size analysis of 316L, 430L and DSS (50%wt 316L+50%wt 430L) powders are given in tables 1 and 2 respectively. Cylindrical green compacts of 30mm diameter and 12mm height were compacted at 560 MPa. Green compacts were sintered at 1350°C for 4 hrs in vacuum at 5x10-2 torr with back filling of argon gas. After sintering, the samples were cooled at the rate of 30°C per minute. Densities of both green and sintered compacts were measured by the mass and physical dimensions. Densification parameter (ΔD) was calculated by using the following formula.

$$\Delta D = (\text{sintered density} - \text{green density}) / (\text{theoretical density} - \text{green density})$$

Microstructural analysis was carried out with the help of image analyzer. Mechanical properties such as tensile strength and hardness of sintered stainless steels were evaluated by using Hounsfield tensometer and Rockwell hardness tester respectively. Structural evolution of the sintered steels was studied by X-Ray Diffractometer (Make: Rigaku, Japan) with Cu-Kα target. Fracture mode of tensile tested samples was evaluated by scanning electron microscopy.

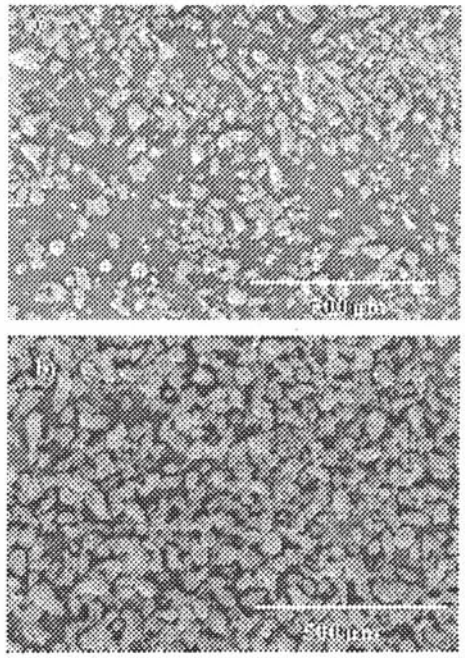

Fig. 1 SEM Micrograph of 316L and 430L powders

TABLE 2 Sieve size analysis of three different stainless steels

Base Powder	Sieve Size					
	90µm	75 µm	63 µm	45µm	37 µm	-37 µm
316L	---	3.25	14.25	21.50	33.50	25.5
430L	---	9.50	28.50	17.25	26.50	17.5
DSS	---	4.25	14.50	19.35	35.50	25.0

TABLE 1
Chemical composition of base powders and powder mix

Base Powder	Elements Concentration (wt %)							Flow Rate 50 g/(sec)	Apparent Density (g/cm^3)
	Cr	C	Ni	Si	Mn	Mo	Fe		
316L	16.60	0.02	12.4	0.90	0.10	2.10	Bal	25.4	2.77
430L	16.56	0.012	0.00	1.20	0.10	----	Bal	27.5	2.88
DSS	16.58	0.018	6.22	1.05	0.10	1.10	Bal	26.5	2.92

3. RESULTS AND DISCUSSION

Figure 2 shows the densities of three different stainless steels sintered in partial vacuum. From the density bar graphs the highest sintered density has been attained for DSS among the three different stainless steels. This higher density is due to the dominant bulk transport mechanisms such as grain boundary and volume diffusion exist between the adjacent particles during longer duration of sintering at very high temperature. The co-ordination number between the adjacent particles in the green DSS compacts are enhanced by the inter locking (closed packing) of the different sizes of 316L and 430L particles [fig.1]. Moreover irrespective of the heating mode; the ferritic particles undergo a higher densification as compared to their austenitic counterparts. This can be attributed to relatively higher diffusivity in the more open body-centered cubic structure of the 430L compacts[1]. Relative percent theoretical densities of DSS, ferritic and austenitic stainless steels are 96.10, 94.4 and 92.25 respectively, which are shown with in the parenthesis in the fig.2. Figure 3 shows the densification parameter for three different stainless steels. The improvement in density in the sintered DSS is approximately 17 to 18 percent from its green condition. Hence higher densification parameter of 0.8040 is exhibited by the sintered DSS. The densification parameter for ferritic grade is 0.7309 and austenitic grade is 0.6451.

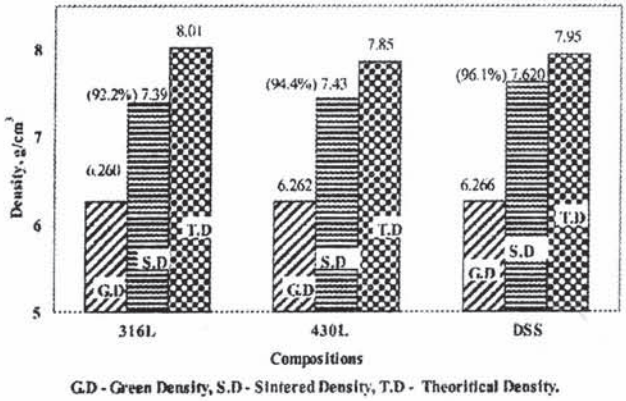

G.D - Green Density, S.D - Sintered Density, T.D - Theoritical Density.

Fig. 2 Densities of Different stainless steels sintered in partial vacuum.

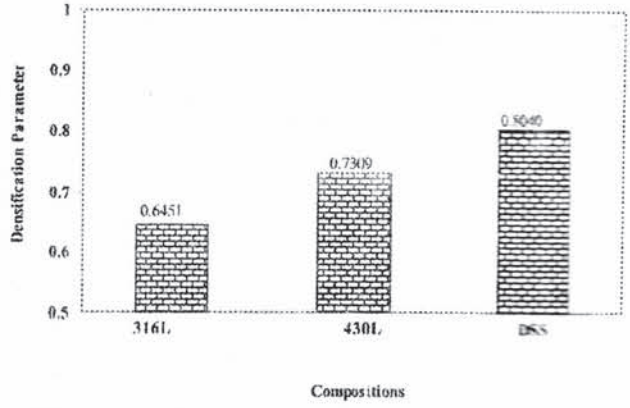

Fig. 3 Densification parameter of different stainless steels sintered in partial vacuum.

Figures 4 and 5 show the microstructures of sintered stainless steels under unetched and etched conditions respectively. Figure 4 exhibits relatively more porosity for 316L and least for DSS. However, the porosity level for 430L is intermediate. From this it is also confirmed that sintered DSS has more density compared to other two stainless steels. The microstructure of the sintered 316L stainless steel consists of polygonal austenitic grains with twins. This twin structure confirms that the stainless steel is free from carbide precipitates. Similarly sintered 430L stainless steel reveals coarse polygonal structure (fig.5b). Sintered DSS (fig.5c) shows the duplex (austenite and ferrite) structure. For both straight 316L and 430L compacts, pores have a relatively more rounded appearance. Higher sintering temperatures and long sintering times produce more pore rounding and grain growth, both of which impart ductility and impact strength to the part [13]. From the 316L microstructure (fig.5a), it can be seen that most of the pores are attached at grain boundaries and some pores are interior. When the pores are attached to the grain boundaries, grain boundary diffusion is the main bulk transport mechanism, which causes the densification of the parts during sintering. During sintering, the interaction between pores and grain boundaries can have three forms: the pores can retard grain growth, the pores can be dragged by the moving grain boundaries during grain growth, or the grain boundaries can break away from the pores, leaving them isolated in the grain interior. As the temperature is increased, the rate of grain boundary motion increases [14]. In general the grain sizes in 316L and 430L stainless steels are coarser than the ferrite grains in the sintered DSS. Moreover in the DSS microstructure, austenite and ferrite phases are almost balanced.

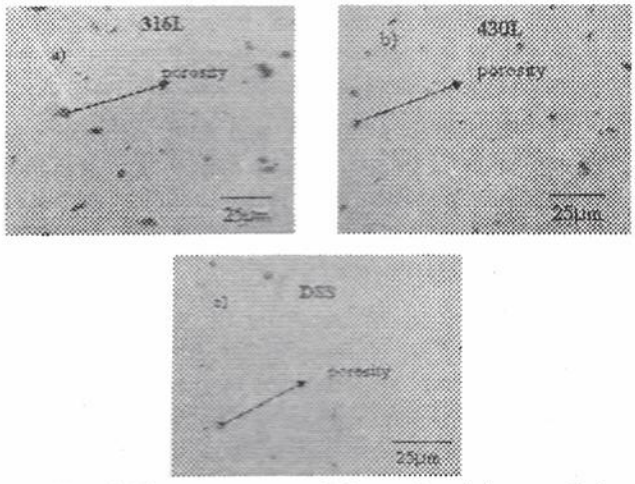

Fig. 4 Microstructures of sintered stainless steels in vacuum atmosphere (unetched condition) a) 316L b) 430L and c) DSS.

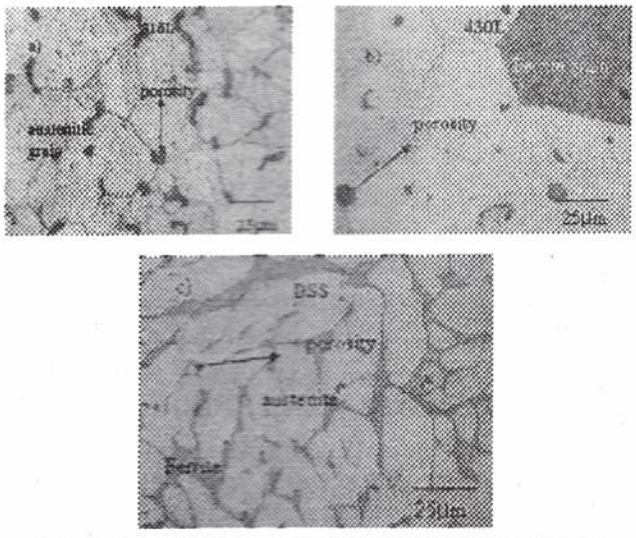

Fig. 5 Microstructures of sintered stainless steels in vacuum atmosphere a) 316L b) 430L and c) DSS.

Figure 6 shows the XRD pattern of sintered DSS. XRD pattern exhibits austenite and ferrite peaks with varying intensities. However, hard peaks such as sigma, carbides are not found. The mechanical properties of the sintered stainless steels are shown in the table 3. Sintered DSS exhibits highest ultimate tensile strength (760 MPa), high yield strength (425 Mpa) and high hardness (67 HRA).

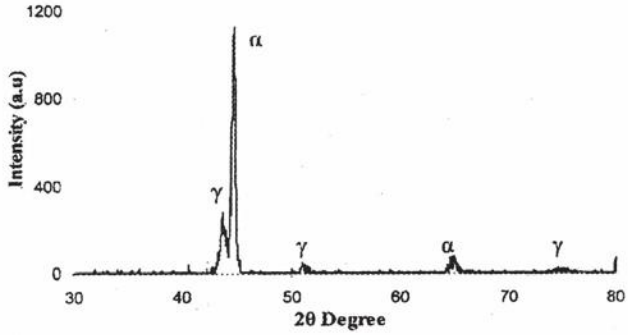

Fig. 6 XRD pattern of sintered DSS in partial vacuum at 1350°C

TABLE 3 Mechanical properties three different stainless steels sintered in partial vacuum.

Composition	Compaction Pressure (560 MPa)				
	Yield strength (MPa)	% Elongation	Hardness (HRA)	Ultimate Tensile Strength (MPa)	Young's Modulus (GPa)
316L	263	33	63	420	88
430L	258	22	61	390	85
DSS	425	12	67	760	120

The ultimate strength of the sintered DSS is approximately twice than that of individual stainless steels. This drastic increment in the tensile strength and hardness of DSS is due to the combination of austenite and ferrite phases, higher density and finer grain size. The grain size of the ferrite in the DSS is finer than the grain size of the ferritic and austenitic stainless steels (fig.5c). Similarly the Young's modulus of the sintered DSS is better than the other stainless steels. Austenitic stainless steel has moderate strength and highest elongation than the other stainless steels. This is due to the longer sintering time at higher temperature. Moreover, lower carbon content in the steel improves the ductility. The stress-strain curves of these stainless steels are given in fig.7. SEM fractographs of the tensile tested samples are given in fig.8. SEM fractographs of 316L and 430L show dimples of various sizes indicating completely ductile mode of fracture. However, DSS exhibits both dimples of various sizes and cleavage features indicating mixed mode of failure (fig.8 c).

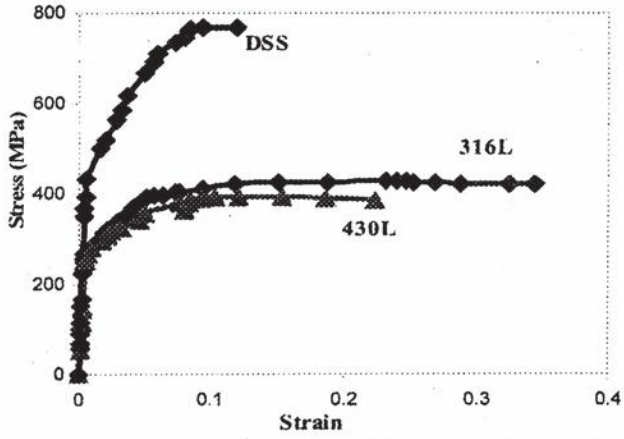

Fig.7 Stress- strain curves for different stainless steels sintered in partial vacuum

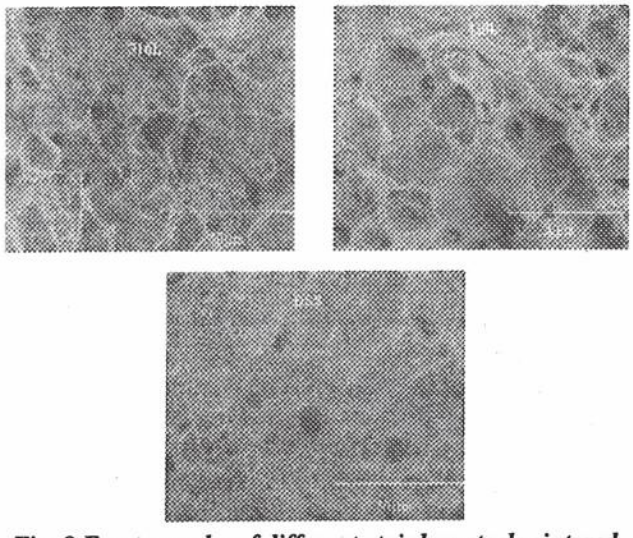

Fig. 8 Fractographs of different stainless steels sintered in partial vacuum.

4. CONCLUSIONS

The results obtained from various studies are presented and discussed. From the results and discussion, the following conclusions are made:

a. Density and Densification parameter of the sintered DSS exhibits highest values after vacuum sintering, i.e 17% improvement in density.

b. The microstructures of 316L, 430L stainless steels reveal their respective structures. Similarly sintered DSS shows the duplex structure (ferrite and austenite). In the sintered DSS microstructure the ferrite and austenite phases are almost balanced.

c. XRD pattern of the sintered DSS confirms the austenite and ferrite peaks.

d. The strength of the DSS is approximately twice (760MPa) than that of the other stainless steels with moderate ductility (12% elongation).

e. The Fractographs of 316L and 430L stainless steels show dimples of various sizes indicating ductile mode of failure, whereas DSS reveals dimples as well as cleavage features indicating mixed mode of failure.

ACKNOWLEDGEMENTS

The authors would like to thank Dr. M. Chidambaram, Director, NIT, Tiruchirappalli-620 015 for providing financial support and permission to present this research paper. Authors would also like to acknowledge the Centre for Nano Materials, ARCI, Hyderabad for providing the facilities to carry out the sintering process.

REFERENCES

1. P. Datta, G.S. Upadhyaya, "Sintered duplex stainless steels from premixes of 316L and 434L powders", Materials Chemistry and Physics Vol. 67, pp.234-24,(2001).

2. L.A. Dobrza ski, Z. Brytan, M. Actis Grande, M. Rosso, E. J. Pallavicini, "Properties of vacuum sintered Duplex Stainless Steels", Journal of Materials Processing Technology, Vol. 157-158, pp.312-316, (2004).

3. P.K. Samal, J. B. Terrell, "Mechanical properties improvement of PM 400 series Stainless Steels via nickel addition", Metal Powder Report December 2001, pp. 28-34, (2001).

4. A. J. Rawlings, H. M. Kopech, H. G. Rutz, "The effect of service temperature on the Properties of ferritic P/M stainless steels", Proceedings of International Conference on Powder Metallurgy & Particulate Materials PM2TEC'97, Chicago USA, (1997).

5. D. Schaefer, C.J. Trombino, "State of North American P/M industry 2005", PM2TEC'2005, Montreal, Canada.

6. C.J. Munez, M.V. Utrilla, A. Urena, "Effect of temperature on sintered austeno-ferritic Stainless steel microstructure", Journal of Alloys and Compounds, (2007).

7. J. Kaziora, M. Nykiela, T. Pieczonkab, T. Marcu Puscasc, A. Molinaric, "Activated sintering of P/M duplex stainless steel powders", Journal of Materials Processing Technology, vol.157–158, pp712–717,(2004).

8. Olena Smuk, "Microstructure and Properties of Modern P/M Super Duplex Stainless Steel", doctoral thesis, Dept. of Mat. Sci. and Eng., Royal Institute of Technology, Sweden, pp1-5, (2004).

9. F. Iacoviello, M. Boniardi, G.M. La Vecchia, "Analysis of stress ratio effects on fatigue Propagation in a sintered duplex steel by experimentation and artificial neural network approaches", International Journal of Fatigue, vol.21, pp.957-963, (1997).

10. M. Camposa, A. Bautistaa, D .Caceresb, J. Abenojara, J.M. Torralba, "Study of the Interfaces between austenite and ferrite grains P/M duplex stainless steels" , Journal of the European Ceramic Society ,vol.23, pp.2813–2819,(2003).

11. S.S. Panda, V. Singh, A. Upadhyaya, D. Agrawal, " Sintering response of austenitic (316L) and ferritic (434L) stainless steel consolidated in conventional and microwave furnaces" Scripta Materialia , vol.54, pp. 2179–2183, (2006).

12. C. García, F. Martín, P. de Tiedra , L. García Cambronero, "Pitting corrosion behaviour of PM austenitic stainless steels sintered in nitrogen–hydrogen atmosphere", Corrosion Science, vol.49, pp.1718–1736, (2007).

13. E. Klar and P.K.Samal, "Powder Metal Technology and applications", ASM International, vol.7, pp.1115 -1117, (1998).

14. C.H. Ji, N.H. Loh , K.A. Khor, S.B. Tor, "Sintering study of 316L stainless steel metal Injection molding parts using Taguchi method: final density", Materials Science and Engineering A, vol.311, pp.74–82, (2001).

STUDIES ON LEAD FREE NANO $Ba_{0.9}Sr_{0.1}TiO_3$ FERROELECTRIC CERAMICS: SYNTHESIS, CHARACTERIZATION AND PROPERTIES

M. Venkata Ramana[1], V.R.K. Murthy[2] and B.S. Murty[1]

[1]Department of Metallurgical and Materials Engineering,
[2]Department of Physics, Indian Institute of Technology Madras, Chennai.

ABSTRACT

The nanocrystalline $Ba_{0.9}Sr_{0.1}TiO_3$ (BST) ceramics has been synthesized by high energy ball milling. X-ray diffraction studies show that these ceramics are tetragonal. The grain size of the powders has been estimated from the XRD patterns, AFM images and TEM images to be 50nm to 80nm. The dielectric constant and loss tangent were studied as a function of temperature. The ferroelectric and piezoelectric properties have been determined as a function of applied electric field. Investigations of the microstructure indicate an increase in grain size from 63 to 90nm when the sintering temperature is increased from 1200 to 1350°C.

1. INTRODUCTION

Since the discovery of ferroelectrics ceramics there has been a continuous improvement of materials and technologies that have led to a significant number of industrial and commercial applications [1,2]. First step in their fabrication is powder preparation. There are two main processing methods: from the mixture of individual oxides and chemical co-precipitation. The choice of method depends on cost, but even more important is the application. Ball milling of the calcined material is necessary for both types of powders to produce the required chemical and optical homogeneity [1]. Besides homogenization of powders, ball milling could be used for mechanochemical activation or mechanochemical synthesis of ceramics powders [3]. Intensive milling in high-energy mills could be a possible solution to these problems. Intensive milling, i.e. mechanical treatment of starting powders, can activate them for sintering process

and consequently reduce temperatures of thermal treatment [4]. Further, mechanical treatment of ceramic powders can reduce particle size resulting in the production of nanocrystalline powders [4], which are the main interest in the current trend of miniaturization of electronic components [1]. Ceramics materials fabricated from nanocrystalline powders can achieve extremely homogeneous microstructures and almost theoretical densities [4].

Barium titanate (BaTiO3; BT) ceramic is a typical ferroelectric material with Curie temperature around 130oC. It is extensively used in multilayer ceramic capacitors (MLCCs), positive temperature coefficient (PTC) thermistors [5] and piezoelectric transducers. As Sr2+ ions are partially substituted at Ba2+ ions in BT, the Curie temperature could be adjusted linearly in Ba0.9Sr0.1TiO3 (BST) system. BST ceramics are considered good candidates for applications in phased array antennas as well as in capacitors, sensors and PTC thermistors [6]. In general, BT and BST ceramics are prepared by the conventional mixed oxide method based on calcining the mixed oxide or carbonate powders. However, the calcined powders usually consist of chemically inhomogeneous particles with large grain sizes. This makes it unsuitable for use as raw material for advanced electronic components. Therefore, other wet chemical processes including coprecipitation, oxalate, sol–gel and novel mechanical activation process has been employed to produce BT powder [7].

In order to have a better understanding of the dielectric properties, ferroelectric and piezoelectric properties with

smaller crystalline size, we have synthesized nanocrystalline Ba0.9Sr0.1TiO3 by mechanical alloying, on which not much work have been reported so far.

2. EXPERIMENTAL DETAILS

The nano ceramic $Ba_{0.9}Sr_{0.1}Ti_{O3}$ samples were prepared through high energy ball milling i.e., mechanical alloying. Stoichiometric amounts of $BaCO_3$, $SrCO_3$ and TiO_2 were weighted with Sr content. The milling was carried out in a Fritsch Pulverisette P5 planetary ball mill at room temperature for different milling times 0, 5, 10, 15 and 20h. Milling has been carried out in with tungsten carbide (WC) milling media at a speed of 300 rpm and a ball-to-powder weight ratio of 10:1. The milling was stopped for 30 min after every half an hour of milling to cool down the system. The powders thus obtained were uniaxially compacted at 100 MPa to form the pellets of the size 5 mm in diameter and 2 mm in thickness. The pellets were sintered at different sintering temperatures (1200-1350^{0}C) for 2 h in air. The measured density of the sintered BST pellets was found to be within 96%–98% of their theoretical value.

The phase identification was carried out using an x-ray diffractometer (Philips, PW-1710 XRD) with Cu Kα radiation λ=0.15418 nm. The flat polished surfaces of the sintered pellets were electroded with high-purity silver paste and then dried at 423K before making electrical measurements. The electrical measurements were made using a HIOKI-3535 LCR HiTester under a weak electric field (with the maximum magnitude of 1V) in the temperature range of 25-150^{0}C at different frequencies varying from 100 kHz to 100 MHz at a heating rate of 2°C/min. The average crystallite size was calculated from x-ray peak broadening using the Scherer formula after eliminating the instrumental broadening and strain contribution, which was confirmed by transmission electron microscopy (TEM) using a Philips CM20 microscope and atomic force microscopy (AFM). The ferroelectric hysteresis loops (P-E loops) was measured using Radient technologies ferroelectric test system with virtual ground mode.

3. RESULTS AND DISCUSSION

3.1 Structural Characterization

Fig 1(a) compares the XRD patterns of the starting powder mixture of BST with those subjected to different durations of milling. After 20h of milling, alloying starts and some of the XRD peaks of the starting oxides have vanished. The peaks became increasingly broader with milling time and a number of new broadened peaks appeared. The new peak patterns have tetragonal structure suggesting the formation of a new phase during mechanical alloying of mixtures of oxides. However, to form single phase tetragonal BST, it requires sintering. Fig 1(b) compares the XRD patterns of mechanically alloyed and sintered BST pellets at different temperatures (1200-1350^{0}C). The indexing of XRD peaks and the determination of lattice parameters of BST were carried out using a software package POWD. All these peak patterns depict the formation of a single phase with a tetragonal structure. The results also clearly show that there are no diffraction peaks from impurity phases after sintering. The refined lattice parameters of the tetragonal phase are given in Table 1. As the sintering temperature is increased, the peaks are sharpened suggesting the increase in the crystallite size. The grain growth as a function of sintering temperature of BST nano ceramic is shown in Table 1. As the sintering temperature increases from 1200-1350^{0}C, the crystallite size also increases from ~67 nm to 90 nm. In order to realize the sub-micron microstructure in the sintered ceramics, it is essential to have the nanocrystalline powders as starting milled powders.

Fig. 1 XRD patterns of BST
(a) after different milling times and

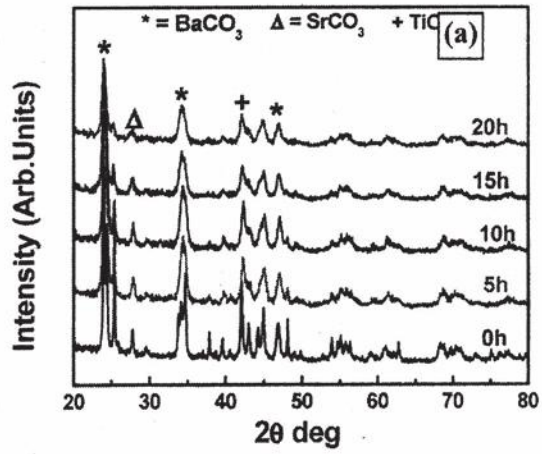

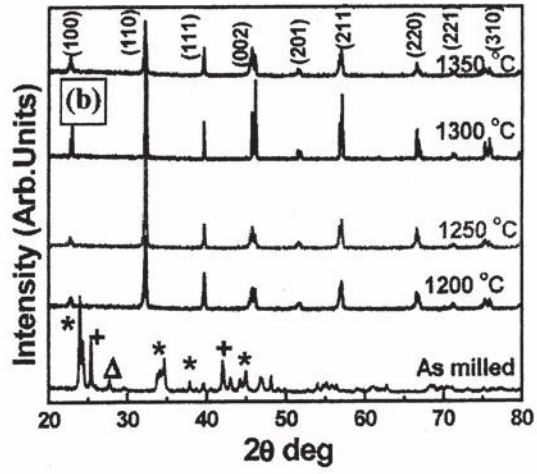

(b) after sintering at different temperatures.

TABLE 1 Properties of nanocrystalline BST prepared by mechanical activation

Parameters	Sintering temperature/2h			
	1200°C	1250°C	1300°C	1350°C
a	3.9982	3.9982	3.9982	3.9982
c	4.1306	4.1306	4.1311	4.1311
c/a	1.0331	1.0331	1.0332	1.0332
V	63.9136	63.9136	63.9136	63.9136
Crystalline size	67	75	83	90
εRT	1393	1427	1175	604
tan δRT	0.02	0.01	0.01	0.02
εTmax	4231	4679	3507	1871
tan δmax	0.05	0.04	0.04	0.05
P_r	0.63	3.64	5.38	6.77
d_{33}	194	210	158	134

The microstructural information on the sintered BST ceramics was obtained using a atomic force microscopy and transmission electron microscopy. Fig 2(a) and (b) show the bright field electron micrograph of the 20h milled sample, the inset shows a selected area diffraction pattern, which clearly established the nanocrystalline nature of the BST. In TEM studies, it is observed that, when the electron beam strikes the polycrystalline agglomerated particles, the agglomerates disintegrate leading to a sea of individual nanocrystalline particles, each one of them being a single nanocrystalline particle. The size of these particles is found to be in the range of 10-30 nm, which is comparable to the crystallite size calculated based on the XRD peak broadening.

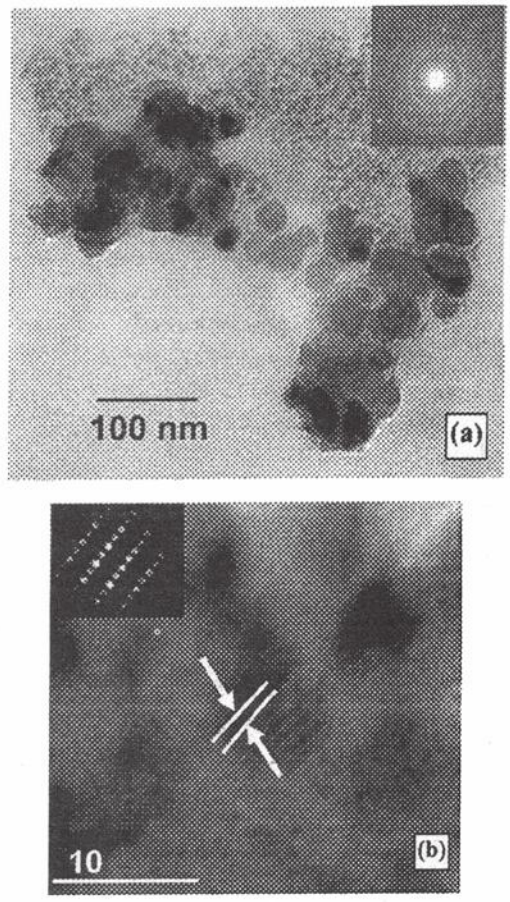

Fig. 2 (a) and (b) TEM bright field image of BST ceramic prepared by mechanical alloying for 20h.

Fig. 3(a) and (b) show the AFM images of nano BST ceramics sintered at 1250oC for 2h. It is observed that the microstructure consists of well developed and

connected grains with very low porosity. The density has reached approximately 97-99% of theoretical density of BST ceramics. The average grain size of the BST nano ceramics is 50-70 nm after sintering, suggesting that the nanocrystalline nature is retained even after sintering.

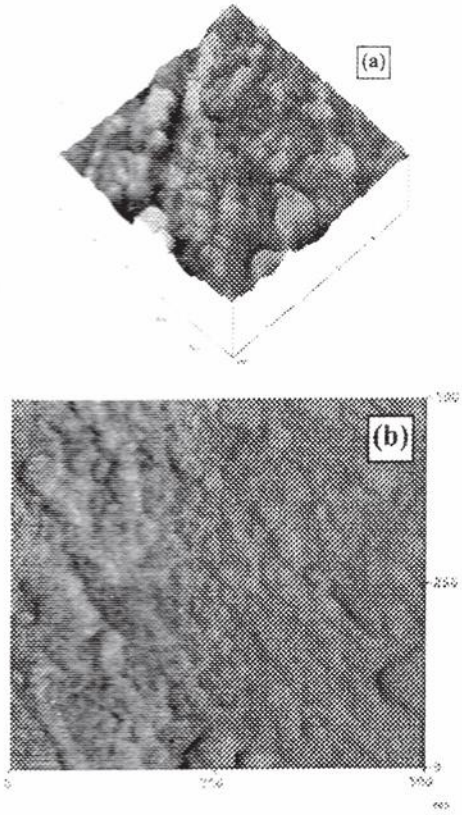

Fig. 3 (a) and (b) AFM images of BST ceramics sintered at 1250oC for 2h.

3.2 Dielectric properties

The dielectric characterization of BST ceramics with different crystallite size as a function of temperature has been investigated. Fig 4(a) shows the dielectric constant of BST nano ceramics as a function of temperature at 100 kHz. It is observed that in all the cases the dielectric constant increases with rise in temperature and reaches a maximum value at a transition temperature (called TC) and then decreases with further increase in temperature. The region around the dielectric peak is broadened [8]. The dielectric constant at the TC was found to be ~ 4231, 4679, 3509 and 1871, respectively, for the BST with grain sizes of for 67, 70, 83 and 90nm. These values are higher than those reported by Patil et al. [9]. The dielectric permittivity of the nanocrystalline samples is remarkably less sensitive to temperature in contrast to the coarse ceramics. This large dielectric constant of mechanically alloyed and sintered samples could be due to the nanocrystalline nature of the BST ceramics, which has shown a crystallite size of 75 nm (Table 1). The dielectric constant can also be analyzed using the dielectric polarizability α_D, which eliminates the effect of the alterations in the unit-cell volume across the solid solution field. The α_D, were calculated using the Clausius-Mossotti relation,

$$\alpha_D = (3/4\pi)\, Vm\, (\varepsilon r - 1)/(\varepsilon r + 2)$$

where V_m=molar volume (=$V_{unit\ cell}$ /Z) and εr is the relative dielectric constant.

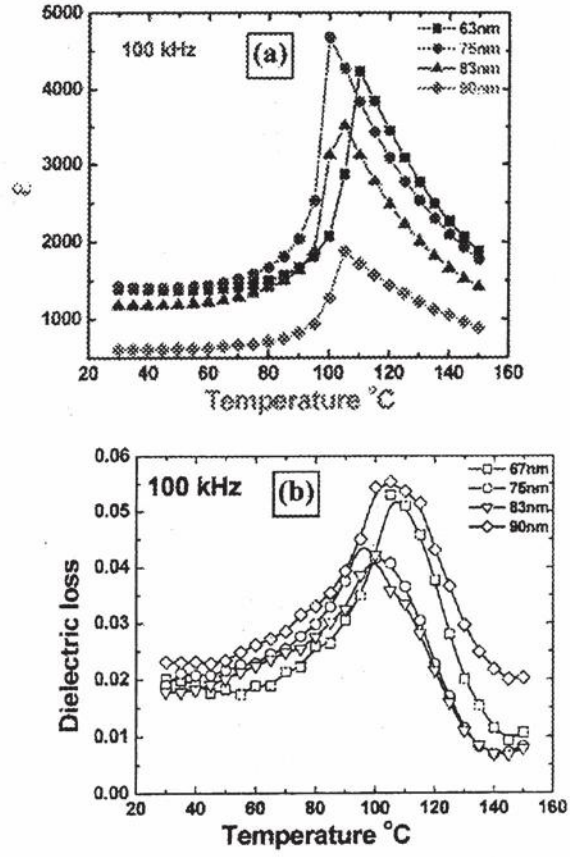

Fig. 4 Temperature dependence of (a) dielectric constant (ε) and (b) dielectric loss (tanδ) for the BST ceramics at 100 kHz.

The dielectric properties of BST ceramics are affected by both crystalline structure of phase and the microstructure. Grain size also has significant effect on the dielectric constant. A ferroelectric single crystal often has a multiple ferroelectric domains separated by interfaces called domain walls, which are transition between different dipole alignments. The dielectric constant is dependent on the population of domains and the mobility of domain walls. It is also believed when the grain size is uniform, the domain wall movement is relatively easy and regular, thus increase

in dielectric constant. When the BST nano ceramic changes its state from paraelectric to ferroelectric state, its crystal structure changes from cubic to tetragonal. Internal stress arises in the material at the Curie transition temperature due to the mechanical deformation of the unit cells that comes from the phase transformation. It is understandable this internal stress is affected by the grain size and uniformity. Uniform grain size generates less internal stress, resulting in easier domain wall motion.

Fig 4(b) shows the dielectric loss behaviour of the BST nano ceramics as a function of temperature at different sintering temperatures. It can also be observed that the loss peak is associated with the phase transition. This is due to the fact that, during phase transition, the domains align themselves and during this process the loss will be high. This is commonly observed phenomena in ferroelectric materials. In general, tangent loss is appreciably increased when temperature rises. The increase in tangent loss (tan δ) is attributed to an increase in the conduction of residual current and absorption current. The tangent loss caused by the dipole movement reaches its maximum at a certain definite temperature. In fact, the rise in temperature and the resulting drop in viscosity exert a double effect on the amount of losses due to the friction of the rotating dipoles: The degree of dipole orientation increases, and at the same time, there is a reduction in the energy required to overcome the resistance of the viscous medium (internal friction matter) when the dipole rotates through a unit angle. The first factor increases PS (spontaneous polarization) and therefore the tangent loss and the second decrease these magnitudes. The dielectric loss values are low (0.02-0.07) for the nano BST ceramic studied in the present work, which renders these materials suitable for practical applications.

The grain size dependence of the polarization (P) and the coercive electric field (Ec) of nano BST ceramics are shown in Fig. 5. It is found that the maximal polarization with an applied voltage of 10V gradually increased as the grain size in the BST nano ceramics increased from 65 to 90 nm. Among many properties that have been reported, the ferroelectric properties have great connection with grain size of the ceramics [10,11]. All these values are in good agreement with the reported results for bulk BST ceramics [12].

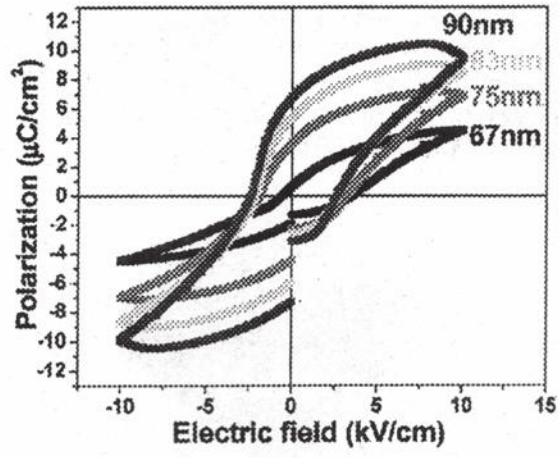

Fig. 5 The hysterics loops (P-E loop) for BST ceramics with different grain sizes at room temperature.

Fig. 6 shows the data on piezoelectric coefficient (d33) of nano BST ceramics as a function of sintering temperature. From the figure it is clear that, the piezoelectric coefficient increases with increase in sintering temperature from 1200-1250°C, after which it decreases with further increase in temperature. This is mainly related to the increase in density. However, both piezoelectric coefficient and dielectric constant (inset in Fig. 6) decrease with increase in sintering temperature after 1250°C, mainly due to completion of optimum densification at 1250°C, and there after there is a decrease in density and followed by grain diffusion. According to the space-charge theory [13], when the grain size increases, the surface area of space-charge layer decreases and simultaneously space charge field will decrease. In such cases, domain walls are free in layer grains and denser ceramics, and the piezoelectric coefficient as well as dielectric constant increases for the pellets with higher density. Higher value of dielectric constant (ε = 1427) and piezoelectric coefficient (d33 =210) at room temperature were obtained by mechanically activation route as compared to conventionally prepared BST [9].

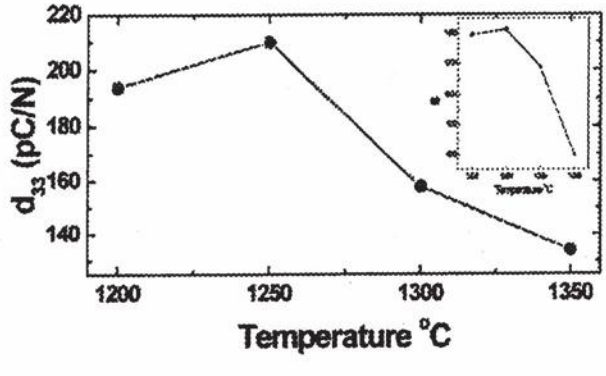

Fig. 6 Variation of piezoelectric coefficient (d33) with sintering temperature of BST nano ceramics.

4. CONCLUSIONS\

1. BST nano ceramic of an average grain size of 30nm with composition of Ba0.9Sr0.1TiO3 has been synthsised by the mechanically activated process.
2. Full dense BST nano ceramics with 99% of theoretical density have been achieved from the partially reacted mixture at a sintering temperature of about 1250oC for 2h.
3. The good dielectric constant, ferroelectric, and piezoelectric properties of the sintered BST nano ceramics measured in the present work indicate that high energy ball milling process is a promising and flexible technique for the preparation of BST nano ceramics.

REFERENCES:

1. G.H. Haertling, J. Am. Ceram. Soc. 82 (1999) 797.
2. N. Setter, R. Waser, Acta Mater. 48 (2000) 151.
3. J. Xue, D. Wan, S.-E. Lee, J. Wang, J. Am. Ceram. Soc. 82 (1999) 1687.
4. Z. Brankovic, O. Milos˘evic, D. Uskokovic, D. Poleti, Lj. Karanovic, Nanostruct. Mater. 2 (1994) 149.
5. B. Huybrechts, K. Ishizaki, M. Takata, The positive temperature coefficient of resistivity in barium titanate, J. Mater. Sci. 30 (1995) 2463–2474.
6. H.Y. Chang, K.S. Liu, I.N. Lin, Modification of PTCR behavior of (Sr0_2Ba0_8)TiO3 materials by post-heat treatment after microwave sintering, J. Eur. Ceram. Soc. 16 (1996) 63–70.
7. L.B. Kong, J. Ma, H. Huang, R.F. Zhang, W.X. Que, Barium titanate derived from mechanochemically activated powders, J. Alloys Compd. 337 (2002) 226–230.
8. M. E. Lines and A. M. Glass, Principle and Application of Ferroelectrics and Related Materials (Oxford University Press, Oxford, 1977).
9. D.R. Patil, S.A. Lokare, R.S. Devan, S.S. Chougule, C.M. Kanamadi, Y.D. Kolekar, B.K. Chougule, Mater. Chem. Phys. 104 (2007) 254.
10. G. Arlt, D. Hennings and G. de With, JAP 58 (1985) 1619.
11. H.F. Cheng, JAP 79 (1996) 7965.
12. C.R.K. Mohan and P.K. Bajpai, Physica B, 403 (2008) 2173.
13. K. Okazaki, K. Nagata, J. Am. Ceram. Soc. 56 (1973) 82.

DRY RECYCLING OF REJECTED MOX FUEL PELLETS IN MOX FUEL FABRICATION FOR PFBR

B.Surendra,M.K.Yadav,A.K.Mishra,Mohd.Afzal and J.P.Panakkal

Bhabha Atomic Research Centre Tarapur.

ABSTRACT

Advanced Fuel Fabrication Facility, BARC, Tarapur has been fabricating Mixed oxide (MOX) fuel of various types for thermal and fast reactors. Presently, MOX fuel for Prototype Fast Breeder Reactor (PFBR) is being fabricated through powder metallurgical route involving cold compaction and sintering. MOX fuel pellets of two compositions (Depleted UO_2 –21% PuO_2 and Depleted UO_2 –28 PuO_2) are being used for PFBR.

Efforts were made to adopt the dry recycling technique to fabricate MOX fuel pellets for PFBR from rejected MOX fuel pellets from earlier fabrication campaigns and MOX fuel pellets for PFBR have been fabricated successfully. In this technique, rejected sintered MOX pellets were pulverized by thermal treatment in oxidizing atmosphere followed by reduction and enrichment adjustment was carried out to form the powder feed for pelletisation of PFBR fuel. This paper presents the details of dry recycling technique, the results obtained and our experience during the fabrication of MOX fuel for PFBR.

1. INTRODUCTION

During the manufacture of MOX fuel, pellets are rejected due to physical defects and low density. Up to 20 wt% of Clean Reject Oxide (CRO) could be successfully recycled back in fabrication process using dry recycling technique(1) for fabrication of MOX pellets thermal reactors. Because of the storage problems associated with plutonium, extensive trials for increased percentage of CRO powder were conducted. A dry recycling technique was developed which was proven on production scale during fabrication of MOX fuel for FBTR(2,3).

Efforts were made to put back the CRO generated during fabrication of MOX fuel of lower plutonium content, into the process for making MOX fuel pellets for PFBR using dry recycling technique. MOX fuel pellets for PFBR were fabricated using this route in plant scale. The physical and chemical specifications of PFBR fuel pellets are as shown below

Sl.No	Characteristics	Specifications
1.	Outer Diameter of the pellet	5.55 ± 0.05 mm
2.	Length of the pellet	7.0 mm (nominal)
3.	Density	94 ± 2 % TD
4.	PuO2 Enrichment (nominal)	21% & 28%
5.	Total Concentration of impurities	< 5000 ppm

This paper describes in detail the experience gained during fabrication of MOX fuel pellets for PFBR from MOX CRO using dry recycling technique. In this technique, rejected sintered pellets were pulverized by oxidation and reduction followed by mixing of desired wt% of PuO_2, 1.0 wt% Polyethylene Glycol (PEG) and 0.8 wt% Oleic Acid (OA) and milled to form the feed for MOX fuel pellets fabrication for PFBR(4).

EXPERIMENTAL

CRO is received in form of rejected sintered MOX pellets. The CRO was converted into powder form to fabricate the MOX fuel pellets for PFBR using dry recycling technique.

PULVERISATION AND POWDER PROCESSING:

In this technique, CRO was pulverized at 700°C for 4 hours in presence of air in electrical resistance heating furnace. Oxidized CRO is then reduced at 700°C for 4 hours in presence of (N_2 + 7 vol% H_2) atmosphere in electrical resistance heating furnace and the reduced CRO powder was used for the fabrication of MOX fuel pellets for PFBR.

PELLETISATION:

A batch of 5 Kg of MOX powder was prepared using

reduced CRO powder along with required quantity of PuO_2, 1% PEG as binder, 0.8% OA as lubricant followed by milling in the Attritor for 60 minutes.

The milled CRO powder was pre-compacted at 75 MPa in double acting hydraulic press and these pre-compacts were granulated in oscillatory granulator. Experimental trials were conducted to find suitable plunger size for compaction. Granules were final compacted in rotary press with plunger size of 6.3 mm diameter to get PFBR size pellets with good integrity and density. Sintering of pellets was done at 1600°C for 6 hrs in presence of (N_2 + 7 Vol% H_2) atmosphere in electrical resistance heating furnace.

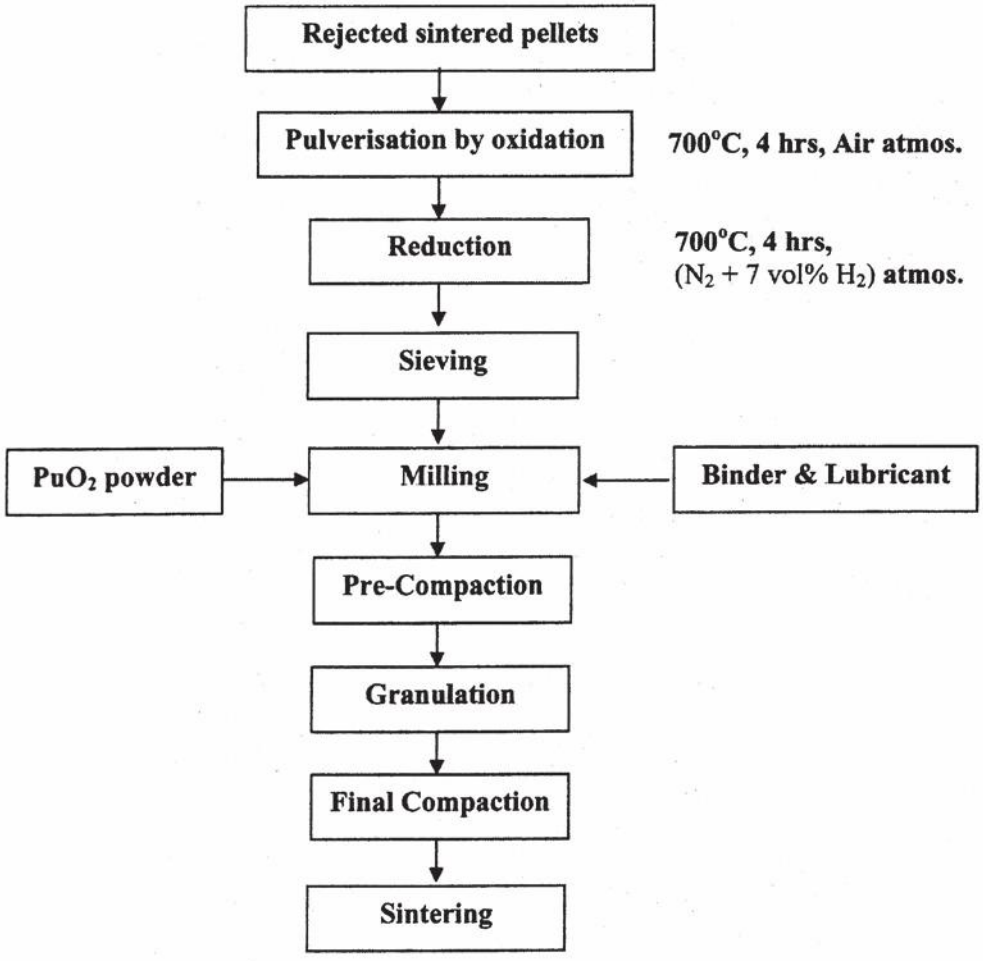

FIG-1: Flow sheet of PFBR MOX fuel fabrication by dry recycling technique

RESULTS AND DISCUSSION:

During the fabrication of MOX fuel pellets for PFBR, CRO powder was utilized by dry recycling technique. Small size plungers, compared to plungers used with virgin powder, were used for the fabrication of PFBR MOX fuel pellets from CRO because of less shrinkage during sintering. The fabricated pellets met diameter and density specifications of PFBR. There was no drastic change in process parameters for the fabrication of PFBR fuel pellets. Presence of plutonium in the material and considering various associated problems in wet recycling;dry recycling technique was preferred in fuel fabrication facility.

ACKNOWLEDGEMENT:

Authors are very thankful to Shri H.S.Kamath, Director, Nuclear Fuels Group, BARC for his keen interest in this work. Authors also wish to thank all the staff members of Oxide Fuel Section for their active support in carrying out this work.

REFERENCES:

1. P.S.Somayajulu, S.K.Shrotriya, Y.G.Nehete, B.K.Shelke, A.K.Mishra, J.P.Panakkal and H.S.Kamath, " Dry recycling of scrap in MOX fuel fabrication", presented in PMAI, Bangalore, 1996.

2. S.K.Shrotriya, B.K.Shelke, B.Surendra, A.K.Mishra, P.S.Somayajulu, Mohd.Afzal, J.P.Panakkal and H.S.Kamath " Recycling of high plutonium bearing pellets on production scale using CRR technique" International conference on Advances in Nuclear Materials, BARC, Mumbai, 2006.

3. P.S.Somayajulu, M.K.Yadav, B.Surendra, A.K.Mishra, Mohd.Afzal, J.P.Panakkal and H.S.Kamath, " Complete Reject Recycling technique in MOX fuel fabrication", International Conference on Characterization and Quality Control of Nuclear Fuel, PMAI, Hyderabad, 2005.

4. S.Mishra, Y.G.Nehete, B.K.Shelke, A.K.Mishra, J.P.Panakkal and H.S.Kamath " Use of Polyethylene Glycol and Oleic Acid in fabrication of nuclear fuel pellets", Transaction of PMAI, Vol-26,1999.

STUDIES ON AA6061-FLY ASH_P COMPOSITES PRODUCED BY PRESS AND EXTRUSION APPROACH

P.R.S. Kumar*, S. Kumaran, T. Srinivasa Rao

Department of Metallurgical and Materials Engineering,
National Institute of Technology, Tiruchirappalli

ABSTRACT

Hot extrusion process was employed to consolidate AA6061-fly ashp composites from mixed powders. The AA6061 powder, developed from elemental powder mixing, and reinforcement powder fly ash were shear mixed in various weight fractions: 0,2,6, and 10 pct. The mixed powders were cold compacted at 345 MPa pressure and finally hot extruded at 500°C with 16:1 extrusion ratio. The optical microstructures, XRD, TEM results show that the composites were effectively alloyed, densified and bonded with fly ash particles. The fly ash particles were distributed uniformly in the matrix in all composites. The density found to be decreased and hardness increased with the increase of fly ash content. All of these improvements are attributed to the merits, including near full densification of the bulk, uniform dispersion of the fly ash particles in the matrix, and strong bonding between the fly ash particles and the matrix alloy resulting from hot extrusion. As compared with matrix alloy, the composites demonstrated a smaller precipitation hardening and elongation, but exhibited a higher Young's modulus. The degradation of precipitation hardening was due to the effect of shape and hollowness of some fly ash particles. The fly ash composites also exhibited a higher wear resistance over that of the matrix alloy.

1. INTRODUCTION

In recent years, research on fly ash as a filler and reinforcement in metal-matrix composites (MMCs) and polymer-matrix composites (PMCs) has been growing. The results of these studies indicate the potential applications of fly ash as a filler or reinforcement in MMCs and PMCs. MMCs exhibit a high specific strength, stiffness and wear resistance, in addition to a service temperature capability, that is much higher than that of other materials or composites. In addition, they are excellent thermal conductors. Therefore, MMCs are now used in, or being considered for use in, a variety of applications, such as connecting rods, automotive drive shafts, cylinder liners and brake rotors [1,2]. However, shortcomings such as unstable fabrication processes and poor workability due to low ductility as well as the high cost of the final product have been a great barrier to their applications in high performance engineering fields [3]. The processes for MMCs can be broadly divided into two categories of fabrication technique: (1) solid state (including powder metallurgy and diffusion); and (2) liquid state (including infiltration, compocasting and spraying). A majority of the commercial applications now empty by liquid state processing. A liquid state process, involving a molten matrix metal, is not only an easy and inexpensive way of making MMCs of a wide variety of shapes, but also a process that can utilize conventional casting facilities and technologies [3]. To obtain MMCs with optimum properties, the fabrication technique has to assure the uniform distribution of the reinforcing material in the matrix and the formation of a good interfacial bond [4].

It is known that secondary processing of discontinuously reinforced composites can lead to the break up of particle (or whisker) agglomerates, to the reduction or elimination of porosity, and to improved bonding, all of which contribute to improve the mechanical properties of MMCs [5]. Amongst the various classical metal-forming procedures, extrusion has been used as the most common secondary processing operation because of its excellent preferential axial alignment of discontinuous particles as well as its large compressive hydrostatic stress state [5,6].

Mechanical properties of composites are affected by the size, shape and weight fractions of the reinforcement, matrix material and reaction at the interface. These aspects have been discussed by many researchers. Guo and Rohatgi [7] reported that with the increase in weight percentages of

fly ash, hardness value increases in Al-fly ash composites, but require higher sintering temperature and sintering times. He also reported that the tensile elastic modulus of the ash alloy increases with increase in fly ash fractions (up to 10wt %). Aghajanian et al. [8] have studied the Al2O3 particle reinforced aluminum MMCs, with varying particulate percentages and reported improvement in elastic modulus, tensile strength, compressive strength and fracture properties with an increase in the reinforcement content. Deuis et al. [9] showed that aluminum-silicon alloys and aluminum based metal matrix composites containing hard particles offer superior operating performance and resistance to wear. Ramachandra and Radhakrishna [10] reported that Al alloy-fly ash composites exhibited better resistance to sliding wear, slurry erosive wear and fog corrosion with increase in fly ash content in the composites. Sudarshan and Surappa [11] have reported that for A356-fly ash composites the bulk hardness, 0.2% proof stress and damping capacity are higher compared to that of the unreinforced alloy.

In the present work, AA6061-fly ash composites were fabricated using a simple cold pressing (Powder Metallurgy) and hot extrusion techniques eliminating the cost effective sintering step. Further, affect of fly ash particles on hardness, tensile properties and wear behavior are investigated.

2. EXPERIMENTAL PROCEDURE

2.1 Material synthesis

The details of elemental metal powders used in this study to make AA6061 (matrix) are presented in Table 1. The powders are supplied by M/s Metal Powder Company, Madurai, Tamil Nadu.

TABLE 1 Characteristics of elemental metal powders

Name of Powder	Purity %	Average Particle Size, mm
Air atomized Aluminum, Al	99.7	63
Magnesium, Mg	99.8	50
Silicon, Si	95.7	05
Copper, Cu	99.0	05
Tin, Sn	99.5	45

The chemical composition of the matrix material used in the experimental investigation is listed in Table 2.

TABLE 2 Chemical composition of AA6061 alloy

Element	Mg	Si	Cu	Sn	Al
Amount, wt.%	1.0	0.6	0.25	0.1	Balance

The reinforcement material used in the present work was fly ash particulates of assorted size with an average particle size of 10 μm. The fly ash was collected from National Thermal Power plant, Visakhapatnam, Andhra Pradesh, India. Particle size was estimated by using computerized particle laser analyzer. The major components of fly ash as received from the source and used for reinforcement are listed in Table 3. The fly ash consists mainly Al_2O_3 ,SiO_2, MgO, Fe_2O_3 and TiO_2. Average fly ash particle density was 2.09 g/cm3.

TABLE 3 Typical chemical composition of fly ash in weight percent

Al2O3	SiO2	MgO	Fe2O3	TiO2	LOI*
30.40	56.41	2.0	8.44	2.75	1.6

* Loss on Ignition

First, the elemental powders were dried at 110 C in an oven for 1 hr and shear mixed in a 1000 g capacity cylindrical jar with the help of a flat blade at 400 rpm for 1 hr. Then, the different weight fractions (2, 6, and 10 wt.%) fly ash powder were mixed with matrix powder in the jar for 1 hr. The powder mixtures were compacted in a hardened steel die at 345 MPa pressure using a universal testing machine (UTM, 100 ton capacity). The compact dimensions were 30 mm long and 30 mm diameter and nearly 50g each in weight. Zinc stearate was used as die wall lubricant. The densities of compacts were determined by weight and volume measurements and that of extruded product were determined by Archimedes principle. The samples were given a protective coating twice to avoid oxidation during extrusion. The samples were then hot extruded with extrusion ratio of 16:1 at 500°C, and graphite as lubricant, without canning and degassing. Extruded bars with 7.5 mm diameter and approximately 250 mm in length were obtained.

2.2 Heat treatment

The extruded samples were solution treated at 535°C for 2 hrs in resistance furnace and quenched down to room temperature with water. Then, they were, immediately aged at 177°C and air cooled for various time durations.

2.2 Mechanical testing

Hardness tests were performed on a Rockwell hardness tester for all the extruded samples. The scale selected for hardness testing was Rockwell E scale, which involves a 1/8" steel ball and 100 kg major load. The reported values of hardness are mean of twelve indentations at different locations on the samples. Tensile tests were performed on a digital extensometer with load cell. The tensile specimens of ASTM E8 standard were used. The strain rate was 1 mm/

min. The reported tensile properties of composites are mean of six tensile tests for each composition. Wear sample of 6 mm diameter and 20 mm length was used for sliding wear test on pin-on-disc machine. The disc of the wear tester was made of EN32 steel with a hardness of HRC 55. The applied load on the specimen against the sliding disc was 1.0 kg. The sliding velocity and sliding distance were 1.0 m/s and 4 km, respectively. The coefficient of friction was obtained by measuring the friction force and dividing it by applied load. The average weight loss was measured using a sensitive balance with an accuracy of 1mg.

2.3 Microstructure characterization

The microstructural characterization of the matrix and fly ash composites were carried out by means of optical microscopy (Image analyzer), scanning electron microscopy (SEM) and transmission electron microscopy (TEM) equipped with energy dispersive x-ray (EDX) unit. The metallographic samples were mechanically ground and coarse polished using emery papers and then polished on a velvet cloth disc using diluted MgO powder as the polishing media. Then the samples were fine polished with 6 μm and 1 μm diamond pastes, finally etched with Keller's reagent [2 ml HF (48 %) + 3ml HCl (conc.) + 5 ml HNO_3 (conc.) + 190 ml distilled water]. In addition, SEM was also used for investigating the wear surfaces.

3. RESULTS AND DISCUSSION

3.1 The microstructure of the composites

The morphologies of elemental powder particles after mixing were shown in fig.1a. The matrix alloy particles primarily exhibit a tear-drop shape, and the size range is quite large (Table 1). The fly ash particulate morphologies were shown in fig.1b, which shows the presence of both cenospheres (round and smoother surfaced particles) and precipitators (porous near spherical particles).

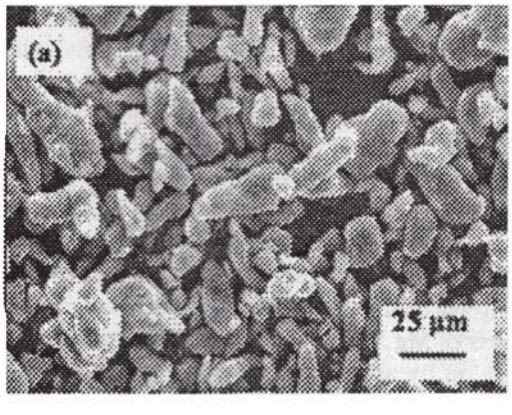

Fig. 1 (a) SEM micrographs of AA6061 matrix alloy powder particles.

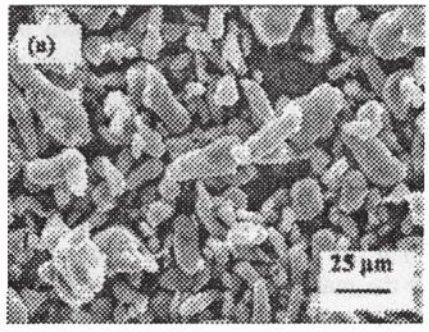

Fig. 1 (b) SEM micrographs fly ash particles

Microstructures of the press-extruded matrix alloy and its composites are shown in fig. 2. The increase in fly ash content is clearly shown from figs. 2(a) – 2(d). With increasing fly ash content, the tendency for the agglomeration of finer fly ash particles was clearly evidenced clearly with 10% fly ash composite.

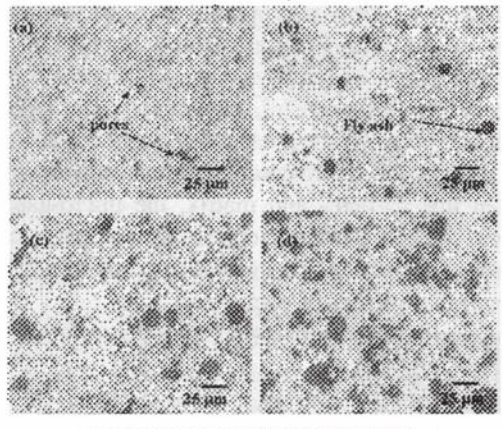

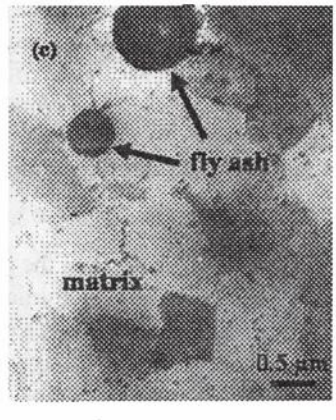

Fig. 2 Optical micrographs of extrusions of (a) AA6061 matrix alloy (b) 2 wt% fly ash composite (c) 6 wt% fly ash composite (d) 10 wt% fly ash composite (e) TEM image of 6wt% fly ash composite

The microstructure of matrix alloy shown in fig. 2(a), clearly indicates that the extent of densification occurred during extrusion as it gives no sign of major pores. Even though the compacts were not subjected to sintering, the extrusion force is high enough to consolidate the powder particles effectively resulting in very limited porosity in the matrix alloy. Also, from the TEM micrograph shown in fig. 2(e) it can be seen that fly ash particle is more intact with the matrix alloy. However, at some locations of microstructures, clusters of smaller fly ash particles and minute pores around them were observed mainly in 6 and 10 wt.% fly ash composites. Slipenyuk et al. [12] showed that when the matrix particle size exceeds the reinforcement particle size, clustering of the reinforcement takes place. In the present investigation, the fly ash particles which are smaller (< 10 μm) in size may be prone to form clusters. The lower density (2.09 g/cc) of fly ash particles also helps in forming clusters. One such clusters has been observed in scanning electron micrograph of 6 wt.% composite shown in fig. 3(a). Corresponding energy dispersive spectrums (EDS) of reinforcement and matrix were also shown in figs. 3(b) and 3(c), respectively. The EDS of fly ash particle confirms the presence of major oxides (fig.3a). Even though, the microstructure shows a clear interface between fine particles and matrix, the micro-gaps were observed around clustered coarse fly ash particles. The presence of such micro gaps would certainly results in poor mechanical properties of composites.

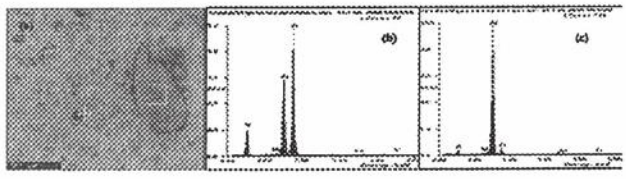

Fig. 3 Photographs of SEM-EDAX showing the (a) fly ash particle clustering (b) EDS analysis of fly ash particle and (c) EDS analysis of interface

The X-ray diffraction (XRD) pattern in the press-extruded condition exhibits the solid solution formation (fig. 4a). Moreover, the formation of Mg_2Si precipitates is evidenced even in extruded condition. Even though the compacts were not subjected to sintering or ageing, the extrusion temperature and time is well enough to form the equilibrium -intermetallic compound (Mg_2Si) in the alloy. Further, heat input might have contributed from interparticle friction and also from frictional forces between compact and die walls. Hence it could be confirmed that the elemental powder mix after extrusion has resulted in alloying. The fly ash composites also exhibited the similar kind of XRD patterns.

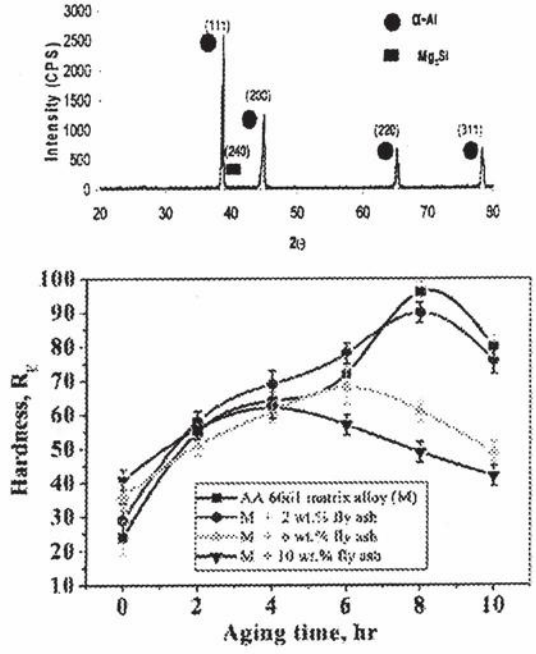

Fig. 4 (a) XRD pattern for AA6061 matrix alloy in the press-extruded condition (b) The aging hardness curves of the AA6061 (M) alloy and the composites

3.2 Age-hardening behavior

The age-hardening curves of the AA6061 matrix alloy and its composites with different weight fractions of fly ash are shown in fig. 4(b). It can be seen that the hardness of all composites are higher than that of the 6061 alloy in the as-quenched condition. The peak hardness and aging responses of the composites are smaller than those of the matrix alloy, and a higher content of fly ash particles has lower peak hardness. Since, there is a large variation in CTE values of fly ash and aluminum alloy, the composites are expected to show enhanced aging kinetics. From literature [Dutta et al, 13] larger the CTE mismatch more favourable is the heterogeneous nucleation sites for stable precipitation. According to Rohatgi [14] during aging of fly ash-A356 composites, diffusion of Mg from the matrix to the fly ash matrix interface was noticed. That means there was every possibility of depletion of Mg from within the matrix to form Mg_2Si precipitate as the fly as content increases. Figure 5 shows the TEM images of matrix alloy and 2 wt.% fly ash composite in aged (T6) condition in which the presence of Mg_2Si precipitates can be seen in matrix alloy (a) and in fly ash composite (b). The energy dispersive X-ray (EDX) analysis between the fly ash particle and the matrix and in the matrix, respectively, is shown in figs. 6 (a) and 6(b). From the EDX of fly ash particle interface Mg peak is clearly seen which indicate its segregation at

the interface leading to less contribution for precipitate formation. That is why the hardness value decreases with fly ash composites in aged condition. Also, hollow cenosphere fly ash particles present in the reinforcement may form weak zone for the propagation of cracks during tensile loading. These may be reasons for inferior age hardening tendency with the increase of fly ash content. Also, studies on age-hardening behavior of AA6061-Al_2O3 composites reported that at peak aging conditions the monolithic alloy exhibited better hardness and strength than composites [15]. Nevertheless, the presence of tin may act to reduce the effective magnesium concentration available to form precipitate phases responsible for hardening [16]. Tin additions may slightly reduce the hardening of the alloy, although benefits associated with enhanced sintering generally outweigh this effect [17].

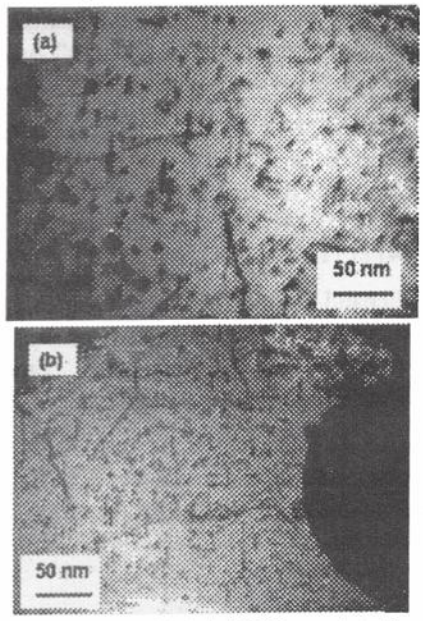

Fig. 5 TEM images of (a) AA6061matrix alloy and (b) AA6061-2wt% fly ash composite after T6-treatement; showing fine Mg2Si precipitates in the matrix alloy and around fly ash particle in the composite

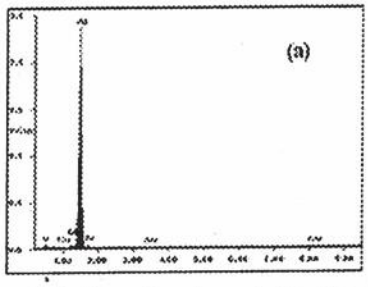

6 EDX analysis from the phase (a) in the matrix of AA6061-fly ash composite and (b) near the interface between the fly ash particle and the matrix of theAA6061-2 wt.% fly ash composite in T6 condition

3.3 The tensile properties

The ultimate tensile strength (UTS) values of the monolithic AA6061 and the fly ash composites in peak aged condition are shown in Table 4. In the present investigation, without loosing ductility value drastically, the AA6061-2wt.% fly ash composite has shown enhanced specific strength due to its lower density. However, the increase in fly ash content beyond 2 wt.% has shown deceleration on aging response because of further depletion of magnesium from the matrix towards fly ash boundaries. Significant increase in young's modulus is observed as shown in Table 4, due to addition of fly ash, which is a major property to be improved in light weight materials.

TABLE 4 The tensile properties of the composites in T6 condition

Material	Young's Modulus (GPa)	0.2% offset Yield Strength, (MPa)	Tensile Strength, (MPa)	Elongation, %
AA6061 matrix alloy (M)	69	298	310	13
M+2 wt.% fly ash composite	71	287	304	11
M+6 wt.% fly ash composite	71	186	206	8
M+10 wt.% fly ash composite	72	181	190	6

3.4 Frictional co-efficients and wear rates

Table 5 lists the coefficients of friction and wear rates of the composites. It can be seen that the presence of fly ash particles increases the coefficient of friction but reduces the wear rate. The improvement of the wear properties of the composites are believed to relate to the strong binding of the abrasive fly ash particles and the matrix. Since the average particle size of fly ash was 10 mm the pull out of particles from the surface was less.

TABLE 5 Wear properties of the composites

Materials	Wear Rate, ($X10^{-3}$ mm^3/m)	Coefficient of Friction, μ
AA6061 matrix alloy (M)	2.73	0.15 to 0.21
M+2 wt.% fly ash composite	2.45	0.38 to 0.42
M+6 wt.% fly ash composite	2.26	0.40 to 0.43
M+10 wt.% fly ash composite	2.13	0.42 to 0.45

Figure 7 shows the wear surfaces of the composites. It can be seen that the ploughing and scoring along the sliding direction is more in fly ash composites. But when compared to the base alloy the wear scars are less due to the presence of fly ash particulates. This shows that the presence of fly ash in the matrix offering resistance to wear. The fractured fly ash particles are seen in the SEM micrographs. The worn debris particles are likely to act as the third body abrasive particles. The fly ash particles trapped between the specimen and the counter face causes a microploughing on the contact surface of the composite.

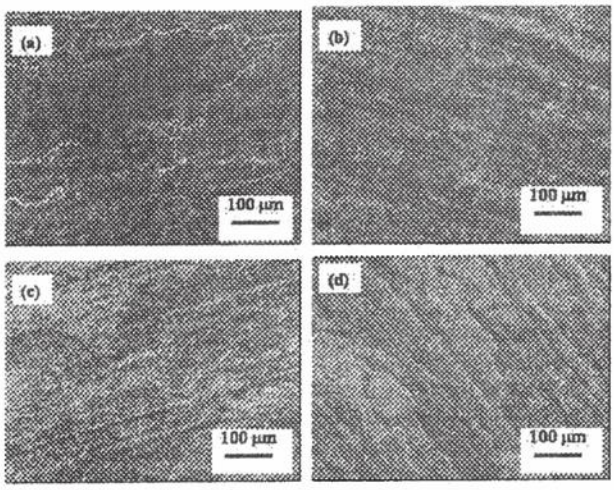

Fig. 7 The wear surfaces of AA6061 alloy and the composites: (a) AA6061 alloy (b) AA6061-2 wt.% fly ash (c) AA6061-6 wt.% fly ash (d) AA6061-10 wt.% fly ash

4. CONCLUSIONS

1. AA6061-2wt.% fly ash composites showed mechanical properties similar to that of AA6061 matrix alloy because of good bonding between the fly ash and matrix alloy. Further increase in fly ash reinforcement resulted in decrease in tensile properties because of clustering of finer fly ash particles.
2. The press-extruded AA6061 matrix alloy revealed the formation of equilibrium compound, Mg2Si even though it was not subjected to sintering in controlled atmosphere.
3. The aging responses of composites are smaller than that of AA6061 alloy. This is attributable to the loss of the precipitation hardenable element, Mg, in the matrix because it migrates to fly ash interface due to its more affinity towards oxygen.
4. The strongly bonded and well dispersed fly ash particles also provide superior wear properties for the composites.
5. The results of the present investigation suggest that press-extrusion approach can be adopted for the production of AA6061-fly ash composites with comparable mechanical properties at cheaper material cost.

ACKNOWLEDGEMENT

The authors would like to thank the Director, National Institute of Technology, Tiruchirappalli, for giving permission to publish this work. The author, P.R.S.Kumar, would like to thank the Department of Technical Education (Govt. of Andhra Pradesh) and AICTE, New Delhi, for sponsoring him to pursue Ph.D. under Quality Improvement Programme.

REFERENCES

1. S. Ho and A. Saigal, "Three-dimensional modeling of thermal residual stresses and mechanical behavior of cast SiC/Al particulate composites", Acta Metall. Mater. Vol. 42, pp 3253-3262 (1994).
2. W.C. Chen, C.H.J. Davies, I.V. Samarasekera, J.K. Brimacombe and E.B. Hawbolt, "Mathematical modelling of the extrusion of 6061/Al2O3/20p Composites", Metall. Mater. Trans. Vol. 27A, pp 4095-4111 (1996).
3. V.J. Michaud, Liquid-state processing, in: S. Suresh, A. Mortensen, A. Needleman (Eds.), "Fundamentals of Metal-Matrix Composites, Butterworth, Guildford/Heinemann", London, pp. 3-22 (1993).
4. H. Lianxi, L. Shoujing, H. Wencan and Z.R. Wang, "Development of the technique of extrusion directly following infiltration for manufacturing of metal matrix composites", J. Mats. Procs. Technol. Vol. 49, pp 287-294 (1995).
5. A.K. Ghosh, Solid-state processing, in: S. Suresh, A. Mortensen, A. Needleman (Eds.), "Fundamentals of Metal-Matrix Composites", ButterwortGuildford/ Heinemann, London, pp 23-41 (1993).
6. C.A. Standford-Beale and T.W. Clyne, "Extrusion and high-temperature deformation of Fibre-reinforced aluminum", Comps. Sci. Technol. Vol. 35, pp. 121-157 (1989).
7. R.Q. Guo and P.K.Rohatgi, "Preparation of Aluminum-fly ash particulate composites by powder metallurgy technique", J. Mater. Sci., Vol. 32, pp 3971 (1997).
8. M.K. Aghajanian, R.A. Langensiepen, M.A. Rocazella, J.T. Leighton and C.A. Andersson, "The effect of particulate loading on the mechanical

behavior of Al2O3/Al metal matrix composites". J. Mater. Sci., Vol. 28, pp 6683 (1993).

9. R.L. Deuis, C. Subramanian, J.M.Yellup, "Abrasive wear of Aluminum composites-a review",Wear, Vol. 201, pp 132 (1996).

10. M.Ramachandra and K. Radhakrishna, "Effect of reinforcement of fly ash on sliding wear erosive wear and corrosive behaviour of Al matrix composites", Wear, Vol. 262, pp 1450-1462 (2007).

11. Sudarshan and M.K. Surappa, "Synthesis of fly ash particle reinforced A356 Al composites and their characterization", Mater Sci Eng A, Vol. 480, pp 117-123 (2008).

12. A. Slipenyuk. V. Kuprin, Yu. Milman, V. Goncharuk and J. ekert, "The effect of matrix to reinforcement particle size ratio (PSR) on the microstructure and mechanical properties of a P/M processed AlCuMn/ SiCp metal matrix composites", Mater. Sci. Eng. A, Vol. 381. pp 165 (2004).

13. I. Dutta, S.M. Allen and J.L. Hafley, Metall. Mater. Trans. A, Vol. 22A, pp 2553-63 (1991).

14. P.K. Rohatgi, J.K. Kim, R.Q. Guo, D.P. Robertson and M. Gajdardziaka-Josifovska Age-hardening characteristics of Aluminum Alloy-hollow fly ash composites, Metall. Mater. Trans. A, Vol. 33A, pp 1541-1547 (2002).

15. Hsu-Shen Chu, Kuo-Shung Liu and Jien-Wei Yeh,"Study of 6061-Al2O3 composites produced by reciprocating extrusion", Metall. Mater. Trans. A, Vol. 31A, pp 2587-2596 (2000), .

16. D. Kent, G.B. Schaffer and J. Drennan, "Age hardening of a sintered Al-Cu-Mg-Si- (Sn) alloy", J. Mater. Sci. Eng. A, Vol. 405, pp 65-73 (2005) .

17. N. Showaiter and M. Youseffi, "Compaction, sintering and mechanical properties of elemental 6061 Al powder with and without sintering aids", Materials & Design, Vol. 29(4), pp 752-762 (2008).